

Effects of vertical grid discretization in infrared transmission modeling

Aldona Wiacek^{*,1}, Kimberly Strong

Department of Physics, University of Toronto, 60 St. George Street, Toronto, Ontario, Canada M5S 1A7

Received 7 January 2007; received in revised form 11 March 2008; accepted 22 March 2008

Abstract

The vertical spacing of a discretization used to model transmission in the mid-infrared spectral range was investigated. The forward model employed in this study is a part of an algorithm used to retrieve trace gas profiles from high-resolution ground-based solar absorption Fourier transform infrared (FTIR) spectra, however, the results have general applicability. A finely spaced retrieval grid was constructed and made progressively more sparse in the troposphere and in the stratosphere. The effect was quantified in terms of transmission differences with respect to the most fine discretization for a suite of molecules (H_2O , O_3 , CO , CO_2 , CH_4 , N_2O , NO , NO_2 , HCl , HF , HNO_3 , ClONO_2 , and N_2) in microwindows commonly used in FTIR spectroscopy. Systematic differences in modeled transmissions are apparent when coarser grid schemes are used for all species and microwindows, though some are below random noise levels typical of spectra recorded at Toronto. The most significant are H_2O and O_3 at 0.30–0.73% and 0.10–0.34%, respectively. CO (0.13%), ClONO_2 (0.84%), and HF (1.03%) are also influenced by the interference of H_2O , which is sensitive to temperature interpolation errors via the lower state energy of the particular H_2O transition. O_3 is a significant interference in CO (0.42%) and ClONO_2 (0.31%) microwindows, but its influence is felt primarily via interpolation errors in the O_3 number concentration profile introduced by the coarser grids. HCl and HF themselves show the next most significant response in transmission to coarser stratospheric grids ($\sim 0.18\%$). Finally, considering transmission differences $>0.1\%$ as significant in typical measurements, we identify maximum tropospheric and stratospheric layer widths that still lead to negligible transmission errors as, respectively, 0.6 and 2.0 km. These numbers can vary depending on the band or transition of interest, the signal-to-noise ratio of the measurement and the use of significantly different *a priori* volume mixing ratio profiles.

© 2008 Elsevier Ltd. All rights reserved.

Keywords: Infrared spectroscopy; Remote sensing; Atmospheric trace gases; Radiative transfer; Vertical retrieval grid spacing; Infrared transmission modeling

1. Introduction

High-resolution ground-based Fourier transform infrared (FTIR) spectra recorded by members of the international InfraRed Working Group (IRWG) of the network for the detection of atmospheric composition

*Corresponding author. Tel.: +41 44 632 3943; fax: +41 44 633 1058.

E-mail address: aldona.wiacek@env.ethz.ch (A. Wiacek).

¹Now at ETH, Institute for Atmospheric and Climate Science, Universitätsstrasse 16, CHN O14, CH-8092 Zürich, Switzerland.

change (NDACC; formerly known as the network for the detection of stratospheric change [1]) have been used to study chemical and dynamical processes in the polar [2,3], mid-latitude [4], and tropical [5] atmosphere in the troposphere, stratosphere, and mesosphere [6,7]. Furthermore, numerous papers using FTIR spectral measurements have been written on, e.g., trace gas trends [8–11], biomass burning emissions [12–15], volcanic emissions [16], and satellite validation [17–20].

Most IRWG members have increased the return from their spectral measurements by performing the retrievals of coarse vertical profiles of trace gases, later integrated to give partial or total column abundances or average volume mixing ratios (VMRs). Information about the vertical distribution of atmospheric trace gases is derived from well-resolved measurements of Lorentz- and Doppler-broadened solar absorption lineshapes. The retrieval approach used by many NDACC stations—including the Toronto atmospheric observatory (TAO)—employs the optimal estimation method (OEM) formulation of Rodgers [21], whereby prior knowledge of the vertical distribution of a trace gas is combined with new information provided by the measured spectra in order to derive the best estimate of the retrieved state. Auxiliary data (*a priori* VMR profiles, pressure and temperature profiles, and spectral absorption line parameters) are used to simulate a spectrum in a suitable microwindow using a multilayer (historically ~29) forward model of the atmosphere. The VMR profile of the target gas is adjusted on all height levels until the forward-modeled and measured spectra match within noise levels. The OEM approach has the advantage of allowing the calculation of retrieval information content [21] and a full characterization of retrieval errors [5,22–26]. The disadvantage of the OEM approach is that information used to constrain the retrieval (i.e. the vertical profile of *a priori* trace gas VMR and its variability) is not well known in some—or all—regions of the atmosphere. Within the IRWG, two vertical profile retrieval algorithms are commonly used: SFIT-2 [22,23,27] and PROFFIT [28], which have been successfully intercompared by Hase et al. [28]. The results presented in this study have been obtained using SFIT-2 v.3.82 (Beta 3).

1.1. Review of previously used vertical discretizations

The vertical grid used in the forward modeling and retrieval process is an implicit retrieval constraint [21] whose choice is left to the user. Table 1 presents the characteristics of a selection of retrieval grids employed in the NDACC/IRWG community, arranged in chronological order. Historically, profile retrievals were performed using as few as 17 vertical layers [29], however, given the continuing computing speed gains, this number is no longer restricted by processing time, although one may want to keep it to a minimum for reasons of computational stability in matrix inversion operations necessary in the OEM approach. In any case, a retrieval performed using 41 layers today [28] is still much faster than a retrieval performed using 17 layers in 1984. It is evident from Table 1 that nearly as many retrieval grids are used as there are investigators in the IRWG, with different total number of layers and upper retrieval boundaries. While the layer width is most commonly ~2 km in the lower stratosphere (15–35 km), it ranges from ~1 to 2 km in the troposphere (0–15 km) and from ~1 to 5 km in the upper stratosphere (35–50 km). In this paper, we systematically explore the effect of tropospheric and stratospheric layer widths on the forward modeling of transmission spectra, however, we make no attempt to find a minimum number of layers or their optimal placement, as this result is not generalizable to all measurement locations, and perhaps more importantly, to all trace gases that one may wish to retrieve.

The choice of the number of layers used in a ground-based FTIR retrieval—and their optimal placement—was discussed in detail by Meier et al. [34], who focused primarily on retrievals of total column amounts using a nonlinear least squares fitting technique. They found that reducing the grid spacing from 2 to 1 km in the troposphere can lead to statistically significant differences in the retrieved total column amounts of tropospheric species in the presence of strong temperature inversion layers in this region; furthermore, they noted that even the retrieved total column of the stratospheric species ClONO₂ can be affected by several percent via the overlapping temperature-sensitive CO₂ feature. Finally, they found that even in the absence of tropospheric temperature inversion layers, the retrieved total column of water vapor can be affected by up to 2.5%. Their preliminary conclusions regarding the grid spacing obtained in the context of profile retrievals, using SFIT-2 v.3.74, were that “the use of an output altitude scheme of constant stepsize throughout the lower atmosphere is found to reduce

Table 1
Characteristics of a selection of vertical retrieval grids reported in the literature

Reference	Station (Instrument)	Layer widths			Tot.	Lid	Algorithm	Target(s)
		T.	L.S.	U.S.				
Rinsland et al. [29]	Kitt Peak (McMath FTS)	2–3	2–3	5–10	17	100	SFIT	NO
Pougatchev et al. [22]	Kitt Peak (McMath FTS)	1	2	5	29	100	SFIT-2	O ₃
Rinsland et al. [23]	Lauder (Bruker 120M), Kitt Peak (McMath FTS)	2	2	2	29	100	SFIT-2	CO, C ₂ H ₆
Notholt et al. [30]	McMurdo (MkIV), Ny Alesund (Bruker 120M)	1	1	1	75	75	GGG	Various
Toon et al. [31]	McMurdo (MkIV)	1	1	1	100	100	GGG	Various
Rinsland et al. [15]	Wollongong (Bomem DA8)	1	2	>2	29	100	SFIT-2	CO, C ₂ H ₆ , HCN
Rinsland et al. [9]	Lauder (Bruker 120M)	2	2	2	29	100	SFIT-2	HCN, CO, C ₂ H ₆ , C ₂ H ₂
Rinsland et al. [10]	Kitt Peak (McMath FTS)	1	2	>2	29	100	SFIT-2	HF, HCl
Barret et al. [24]	Jungfraujoch (Bruker 120HR)	2	2	2	29	100	SFIT-2	O ₃
Rinsland et al. [32]	Kitt Peak (McMath FTS)	2	2	2	29	100	SFIT-2	SF ₆
Barret et al. [20]	Jungfraujoch (Bruker 120HR)	1	≥1		29	100	SFIT-2	CO
Griffith et al. [33]	NIWA (Bruker 120M)	2	2	2	29	100	SFIT	Various
	NPL (Bruker 120M)	1	2	5	29	100	SFIT	Various
Hase et al. [28]	Thule (Bruker 120M), Kiruna (Bruker 120HR)	1.2	1.2–1.5	1.7–3.5	41	82	PROFFIT, SFIT-2	HNO ₃ , O ₃ , N ₂ O, HDO
Meier et al. [34]	Kiruna (Bruker 120HR)	1	2	5	29	100	SFIT/-2	Various
	Wollongong (Bomem DA8)	1.5	1.5	5	29	100	SFIT/-2	Various
Barret et al. [35]	Jungfraujoch (Bruker 120HR)	2	2	2	29	100	Atmosphit	HCl, HF
Schneider et al. [25] ^a	Izana (Bruker 120M)	1.2	1.2	1.3–3.0			PROFFIT	O ₃
Rinsland et al. [36] ^b	Kitt Peak (McMath FTS)	~1	~2	>2	37	100	SFIT-2	CH ₄
Schneider et al. [37] ^a	Izana (Bruker 120M)	1–1.2					PROFFIT	H ₂ O
Wiacek et al. [6] ^b	TAO, Eureka (Bomem DA8s)	~1	~2	>2	41	130	SFIT-2	NO
Wiacek et al. [26] ^b	TAO (Bomem DA8)	~1	~2	>2	38	100	SFIT-2	O ₃ , HCl, N ₂ O
Yamamori et al. [38] ^a	Poker Flat (Bruker 120HR)	2	2	2			SFIT-2	O ₃ , HNO ₃

The layer width (km) given in the troposphere (0–15 km), lower stratosphere (15–35 km), and upper stratosphere (35–50 km) is approximate. The total number of layers and the upper boundary (lid) used in the retrievals are also given in (km).

^aSome grid information inferred from figures.

^bLayer width increases smoothly.

unwanted profile oscillations”. They did not attempt to quantify this phenomenon or identify an optimal width to be used with SFIT-2, only noting that the 1.5-km constant width used in their work “cannot represent the strong gradient in water vapor very well”. In a separate study, Hase et al. [28] reported the inadequacy of a 45-layer grid with a 1.2-km tropospheric layer thickness for optimal estimation retrievals of the vertical profiles of HDO (they noted that the half-width of the features observed in the averaging kernel matrix approached the grid spacing). In the related work of Schneider et al. [37] on vertical profile retrievals of H₂O, a 1-km thickness for the lowest retrieved layer is given, and 1.2-km layers for the lower troposphere can be inferred from the discussion and figures. Finally, while the use of a separate retrieval grid for stratospheric and tropospheric species is evident in the work of Griesfeller et al. [39] (their Fig. 2) the details of how these two grid schemes were constructed are not given. It is therefore the purpose of this work to systematically assess the effect of both stratospheric and tropospheric retrieval layer widths on the transmission levels in forward-modeled spectra of 13 commonly retrieved NDACC/IRWG targets, including water vapor.

2. Radiative transfer: theory and methodology

2.1. Approach to forward modeling of transmission spectra

We modeled transmission spectra using HITRAN 2004 spectroscopic parameters [40] in microwindows typically employed in profile retrievals within the IRWG [41]. The pseudoline list of Toon [41] was used in spectral regions covering the ClONO₂ and HNO₃ absorption features, and mass substitutions were made for all available pseudoline species in these regions. Absorption cross-sections were calculated assuming a Voigt lineshape on a grid of 0.0005 cm⁻¹. Furthermore, solar absorption features were modeled in spectral regions covering the CO, NO, and H₂O (841 cm⁻¹) absorptions [23]. The spectra were modeled assuming boxcar apodization, an ideal instrumental lineshape (ILS) function, a 250-cm optical path difference (OPD), a 45° solar zenith angle (SZA), and a 1.54-mrad field-of-view (FOV), except for spectra in the 750–1350 cm⁻¹ region, where the FOV was set to 4.63 mrad in order to match typical observation parameters. Finally, pressure and temperature profiles were obtained from the National Center for Environmental Prediction (NCEP; using the Goddard Automailer, science@hyperion.gsfc.nasa.gov) and were interpolated onto the 205-level grid scheme that is used internally by the FSCATM ray-tracing algorithm [42], as modified by Meier et al. [34]. The FSCATM internal grid scheme has a spacing of 0.2 km from 0 to 30 km, 0.5 km from 30 to 40 km, 1 km from 40 to 60 km, 2 km from 60 to 80 km, and 5 km from 80 to 100 km. A set of constant *a priori* VMR profiles (Fig. 1) compiled from various sources [26] was also interpolated onto the 205-level grid scheme, and (together with the 205-level NCEP data) served as input to the FSCATM ray-tracing and airmass calculations. The FSCATM program provides as output, density-weighted values of temperature, pressure, and *a priori* VMR profiles in layers whose boundaries were specified, in turn, as given in Table 2. (The choice of layer boundaries is justified further down.) Together with the airmasses, these density-weighted values are direct inputs to the calculations of transmission spectra by SFIT-2. The minimum layer width of 0.2 km was chosen to match the internal (interpolated) layering scheme used by FSCATM. Given the large resultant total number of layers in each grid scheme in Table 2, we stress again that our primary objective was to find the maximum layer width permitted in order to faithfully reproduce transmission spectra, rather than to minimize the overall number of layers, or to find their optimal placement. Nonetheless, by comparing transmission spectra calculated on more sparse grids to those calculated on the most dense grid, an implicit assumption is made that the latter is sufficient to capture all features of the real atmosphere that are of practical consequence for transmission

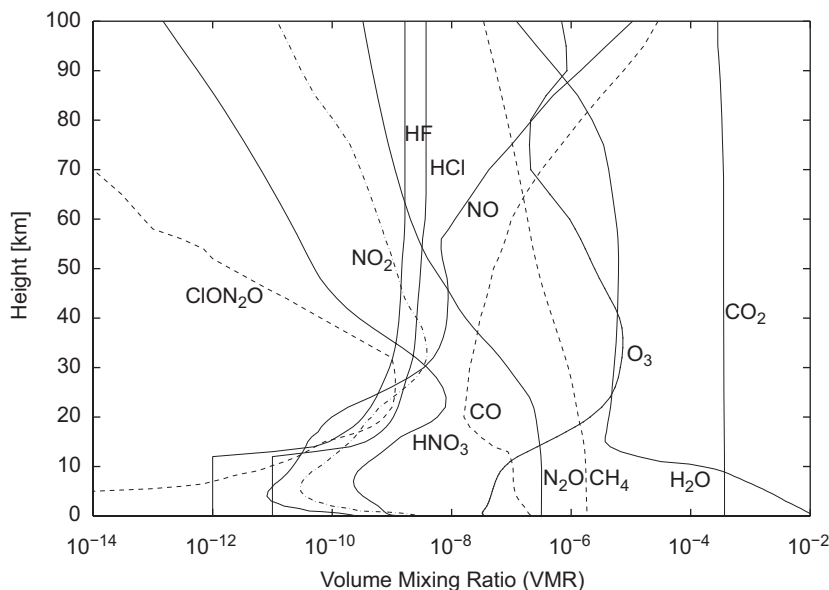


Fig. 1. *A priori* VMR profiles used in this study.

Table 2

Different layer thicknesses (km) that were specified first in the troposphere and second in the stratosphere in order to test the effect of tropospheric (Txxxx) and stratospheric (Sxxxx) layer widths on forward-modeled transmission spectra

Grid scheme	Layer thickness (km) in each region (km)					Total layers in scheme
	0–12	12–36	36–50	50–80	80–100	
T0200	0.2	2.0	2.0	5.0	10.0	87
T0400	0.4	2.0	2.0	5.0	10.0	58
T0600	0.6	2.0	2.0	5.0	10.0	48
T0800	0.8	2.0	2.0	5.0	10.0	43
T1000	1.0	2.0	2.0	5.0	10.0	40
T2000	2.0	2.0	2.0	5.0	10.0	34
S0500	1.0	0.5	2.0	5.0	10.0	76
S1000	1.0	1.0	2.0	5.0	10.0	52
S1500	1.0	1.5	2.0	5.0	10.0	44
S2000	1.0	2.0	2.0	5.0	10.0	40
S2500	1.0	2.5	2.0	5.0	10.0	38
S3000	1.0	3.0	2.0	5.0	10.0	36

calculations. While there is certainly variability in atmospheric profiles of temperature, pressure, and trace gas VMRs on scales less than 0.2 km, this variability is also smoothed by NCEP analyses and our *a priori* VMR profile set. In order to assess the effect of using more dense sources of temperature, pressure, and VMR information in this context, e.g., from sondes, a separate study beyond the scope of this work would be necessary. However, given that the vertical resolution of the ground-based solar absorption FTIR profiling technique is very coarse (~5–10 km, and in some cases worse), studying the effects of small-scale atmospheric variability on transmission spectra is not of practical interest. Our study, on the other hand, is relevant in that it addresses the ability of a given grid scheme to capture the gross features of the atmosphere (VMR, temperature, and pressure profiles) to which the ground-based solar absorption FTIR technique has some sensitivity to.

As already alluded to, a change in the vertical discretization scheme will have an effect on transmission spectra via changes in profiles of atmospheric temperature and pressure (Fig. 2) as well as of trace gas VMR (Fig. 3). (These profiles are all density-weighted in the layer-based representation of SFIT-2 and plotted as a function of layer midpoint. For a detailed discussion of layer- vs. level-based atmospheric representation, see Hase et al. [28].) The primary effect of temperature and pressure on transmission spectra is via perturbations to temperature- and pressure-dependent spectroscopic parameters, as outlined below. While an altered temperature and pressure will also have an effect on refraction and hence on ray-tracing calculations, affecting the relative airmass and the partial column of air in each atmospheric layer (mol cm^{-2}), we found this effect to be very small, at least for the relatively low SZA of 45° used in our study. On the other hand, an altered VMR profile affects the number concentration profile, ρ , of a trace gas (mol cm^{-3}) more directly than pressure or temperature, which only act via the airmass; the number concentration profile is calculated as the product of the VMR and the partial column of air profiles, divided by the profile of layer widths (cm). Lastly, the wavenumber-dependent transmission, $\tau(\bar{\nu})$, between the top of the atmosphere (TOA) and the surface, defined as the exponential of the negative of the total optical depth, is affected via the following equation:

$$\tau(\bar{\nu}) = \exp\left(-\int_{TOA}^0 \rho k(\bar{\nu}) ds\right), \quad (1)$$

where $k(\bar{\nu})$ is a given molecule's absorption coefficient ($1/(\text{mol cm}^{-2})$) and s is the slant path distance (cm). The absorption coefficient $k(\bar{\nu})$ is modeled as the product of the temperature-dependent line strength $S(\bar{\nu}_0, T)$ ($\text{cm}^{-1}(\text{mol cm}^{-2})^{-1} = \text{cm mol}^{-1}$) of the central wavenumber $\bar{\nu}_0$ (cm^{-1}) with the broadening (or lineshape) function $f(\bar{\nu} - \bar{\nu}_0)$ ($1/\text{cm}^{-1}$), normalized as per Eq. (3):

$$k(\bar{\nu}) = S(\bar{\nu}_0, T)f(\bar{\nu} - \bar{\nu}_0), \quad (2)$$

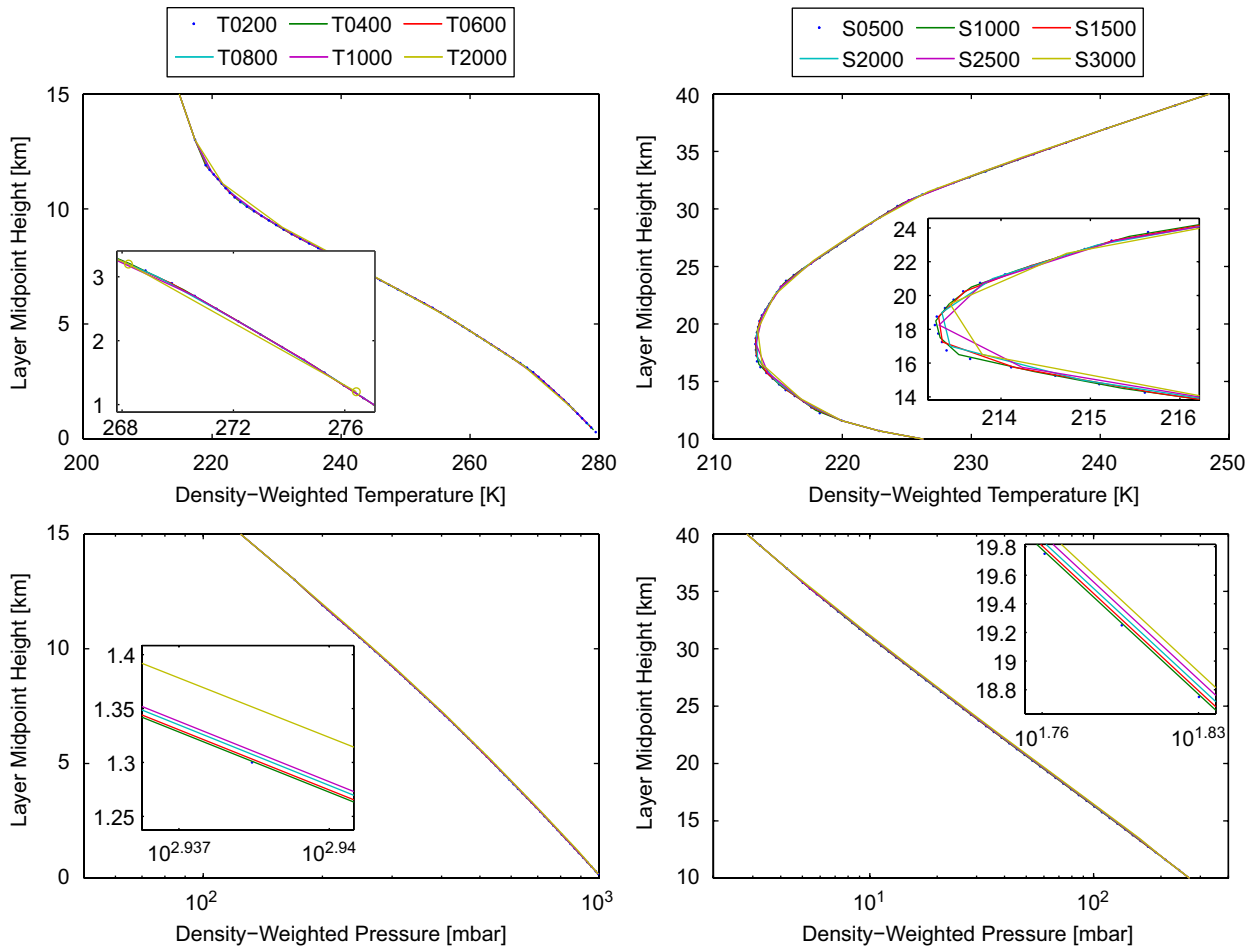


Fig. 2. Mean density-weighted temperature (top) and pressure (bottom) profiles above Toronto, based on 362 NCEP analyses, for tropospheric (left) and stratospheric (right) grids.

$$\int_{-\infty}^{\infty} f(\bar{\nu} - \bar{\nu}_0) d\bar{\nu} = 1. \quad (3)$$

For a detailed discussion of line strength and line broadening mechanisms see, e.g., [43, Appendix A] or [44] and references therein. For the purposes of our work, we emphasize that S is temperature-dependent, more so when the lower state energy (E'') of the corresponding quantum mechanical transition is high, and it is defined as

$$S(\bar{\nu}_0, T) = S(\bar{\nu}_0, T_0) \frac{Q(T_0) \exp(-hcE''/(kT)) (1 - \exp(-hc\bar{\nu}_0/(kT)))}{Q(T) \exp(-E''/(kT_0)) (1 - \exp(-hc\bar{\nu}_0/(kT_0)))}, \quad (4)$$

where T_0 is a reference temperature of 296 K, Q is the partition function, h is the Planck constant, c is the speed of light, and k is the Boltzmann constant (not to be confused with $k(\bar{\nu})$ in Eq. (2)). As noted previously, the lineshape (or broadening) function employed by SFIT-2 is the Voigt function, which is a convolution of the Lorentz and Doppler lineshape functions. It takes as inputs the Lorentz and Doppler line broadening coefficients, $\gamma_L(T, p)$ and $\gamma_D(T)$, respectively, which are themselves a function of temperature (T) and pressure (p):

$$\gamma_L(T, p) = \left(\frac{T_0}{T}\right)^{n_{\text{air}}} [\gamma_{\text{air}}(T_0, p_0)(p - p_s) + \gamma_{\text{self}}(T_0, p_0)p_s], \quad (5)$$

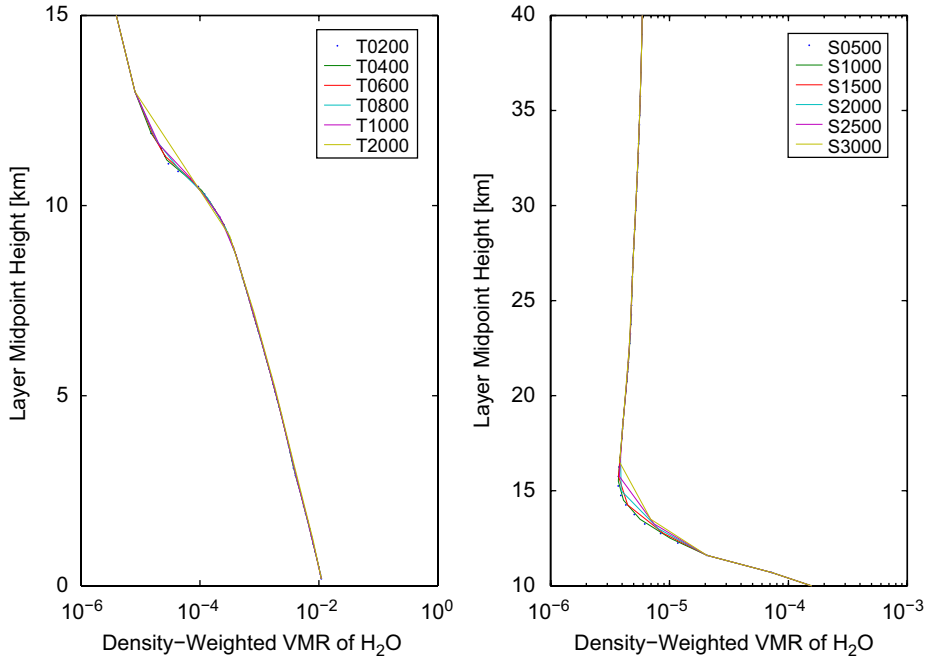


Fig. 3. Mean density-weighted VMR profile of H₂O above Toronto for tropospheric (left) and stratospheric (right) grids.

$$\gamma_D(T) = \sqrt{\frac{2kT\bar{v}_0}{M c}}. \quad (6)$$

γ_{air} and γ_{self} (cm⁻¹ atm⁻¹) are the air- and self-broadening coefficients, also measured at $T_0 = 296$ K and $p_0 = 1$ atm, p_s is the partial pressure of the gas, n_{air} is the exponent of the temperature dependence of the broadening coefficients, and M is the molecular mass of the species in question. We can see from Eq. (5) that the VMR profile, which determines the partial pressure of a gas, will have a small feedback on the Lorentz broadening coefficient via p_s .

2.2. General features of transmission spectra

In order to separate changes in transmission due to the grid spacing from those due to the typical annual variation of temperature and pressure profiles (the *a priori* VMR profiles were held constant throughout this study) 362 spectra were simulated for each grid scheme using 362 density-weighted temperature and pressure profiles derived from the 362 NCEP pressure and temperature analyses available for Toronto in 2004. Fig. 4 shows the annual mean and standard deviation of transmission *differences* with respect to the most dense tropospheric grid (T0200) for a microwindow containing a highly temperature-dependent water absorption feature. The inset shows the same quantities for an ozone microwindow, where the transmission differences due to tropospheric grid changes are much smaller and highly pressure broadened, as expected. More surprising is that even these much smaller annual average transmission differences are clearly separated from one another. Unless otherwise noted in Section 3, this is the case for all gases, especially at and near line center. To reduce the computational burden of the transmission simulations, for the case of H₂O, we experimented with sampling every second, third, fourth, etc., spectrum in the 362-member ensemble in order to produce a representative annual mean transmission difference and its $\pm 1\sigma$ spread. We settled on using every fifth spectrum for H₂O (Figs. 5 and 6), as well as for all the other trace gases (Figs. 10–22). These figures are all arranged as follows. The top panels show the annual average transmission (%) in a given microwindow for the most dense tropospheric (left) and stratospheric (right) grid schemes. (Average transmissions for different grids are not distinguishable on this scale.) The bottom panels show the annual average transmission *difference*

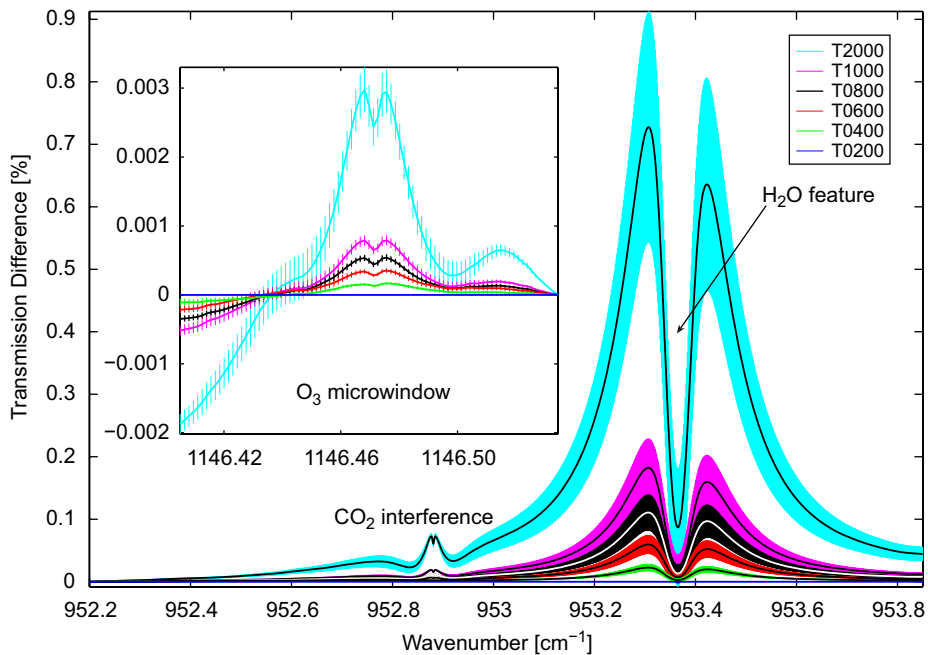


Fig. 4. Annual average transmission differences (solid lines) in H₂O and O₃ (inset) spectral absorption regions due to less dense tropospheric grid spacings (with respect to the T0200 scheme). Error bars (blending into a shaded region for H₂O) show the $\pm 1\sigma$ spreads in these average transmission differences due to annual fluctuations in temperature and pressure.

(%) due to a given grid scheme with respect to the most dense grid scheme in the troposphere (left panel; e.g. $(T2000 - T0200) * 100$) and in the stratosphere (right panel; e.g. $(S3000 - S0500) * 100$). The transmission difference due to the most dense tropospheric (T0200) or stratospheric (S0500) grid scheme is also shown with respect to itself (since it is always zero in either figure panel it helps to guide the eye). In all figures, the number in the legend of the left panel refers to the layer thickness (m) between 0 and 12 km, while the number in the legend of the right panel refers to the layer thickness (m) between 12 and 36 km. Finally, all grids that are varied in the troposphere (stratosphere) have a constant 2.0 km (1.0 km) layer thickness in the stratosphere (troposphere), with remaining grid details given in Table 2.

The choice of a 12-km tropopause height is based on mean HALOE measurements above Toronto [26], which show it at ~ 10 km in the winter and at ~ 14 km in the summer, with an annual mean height of ~ 12 km. The transition in grid spacing again at 36 km is a somewhat arbitrary division between lower and upper stratosphere, following values used previously by others (Table 1); it coincides with the VMR peak of the O₃ profile above Toronto, also derived from coincident HALOE measurements. Above 36 km, the partial column contribution is small for all gases except NO [6], whose VMR profile increases exponentially with height, and NO₂. In particular, by 36 km, the O₃ number concentration profile (not shown) decreases again to $\sim 25\%$ of its peak value attained at ~ 22 km; for comparison, at 36 km NO₂ decreases to 37% of its peak at 28 km, while at the same height NO decreases to only 76% of its peak, which is found at 32 km. While it is expected that variations in layer thickness between 36 and 50 km would lead to some transmission differences, we expect these to be small for two reasons. The first is that there are no further maxima in the number concentration profiles (which are a better indication of the contribution to the total column than the VMR profiles) of all three gases in this region, and the second is that there is a roughly constant gradient in temperature up until the stratopause is reached at ~ 50 km. If NO in the mesosphere-lower-thermosphere is of interest, then the grid spacing in this region should be investigated further, considering the radiative transfer problem more fully, i.e. including emission effects as well as the effects of non-local thermodynamic equilibrium on emission.

3. Results

3.1. Transmission differences of selected H_2O and CO_2 transitions

Fig. 5 shows the effects of tropospheric and stratospheric grid variations on an H_2O absorption feature at 841.9028 cm^{-1} , which has a lower state energy (E'') of 552.9 cm^{-1} . As expected, stratospheric grid variations between 12 and 36 km lead to extremely small average transmission differences ($<0.001\%$) that are not distinguishable from one another near the H_2O line center. Other sharp but very small transmission differences are due to minor absorptions by O_3 and CO_2 , as indicated. Tropospheric grid variations, on the other hand, produce highly pressure-broadened transmission differences of up to 0.302% (T2000). In order to detect this systematic feature with a relative signal-to-noise ratio (SNR) of at least 2 near the line center, a spectrum would need to be recorded with an SNR of 662 ($= 2 * 1/0.302\%$). (The value 2 is somewhat arbitrary and different criteria could be applied here.) Depending somewhat on location, season, and specific meteorological conditions, an SNR of 600 fits quite comfortably within the limits of FTIR observation capabilities. We note that we are referring to an SNR which is calculated from the residuals of spectral fits, and which therefore includes both random (e.g. instrumental) and systematic (e.g. spectroscopic) errors. Purely random errors in FTIR measurements are much smaller and lead to SNRs of several thousand. In any case, the transmission differences are big enough in this case that two side-by-side investigators using the same spectroscopic parameters as well as the same temperature, pressure, and *a priori* VMR profiles will introduce systematic differences of up to 0.302% into transmissions calculated for the first iteration of the retrieval process—if using the different retrieval grids introduced above.

The shape of the transmission differences due to tropospheric grid changes in Fig. 5 is a mixture of a highly pressure-broadened difference in the line wings and a less broadened difference in the line core. It is easy to see from Fig. 3 that there are differences in the density-weighted *a priori* VMR profile of H_2O just below the 12-km tropopause, which are consistent with the calculated transmission difference near the line center: a smaller VMR on grid T0200 will result in a greater transmission than from the larger VMR on grid T2000, finally leading to a negative transmission difference near the line center in Fig. 5. As far as the lower portions of the *a priori* VMR profile are concerned, after some magnification (not shown) it is possible to see that the VMR on grid T0200 is again slightly smaller than that on grid T2000. This would again lead to a negative

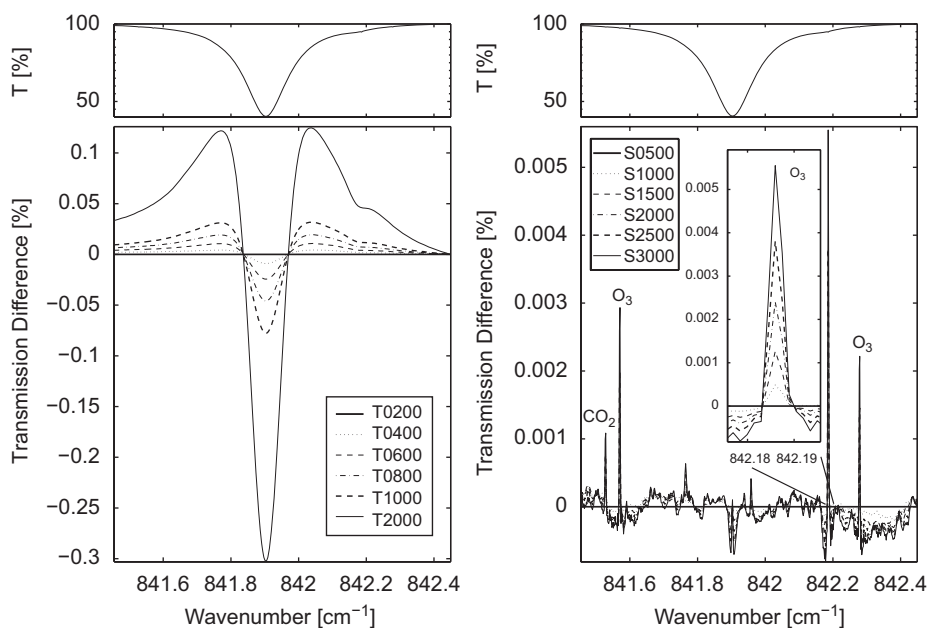


Fig. 5. Transmission (top panels) and transmission difference (bottom panels) for tropospheric (left) and stratospheric (right) grid spacing variations in the 841.9 cm^{-1} H_2O microwindow ($E'' = 552.9\text{ cm}^{-1}$). See text for legend details.

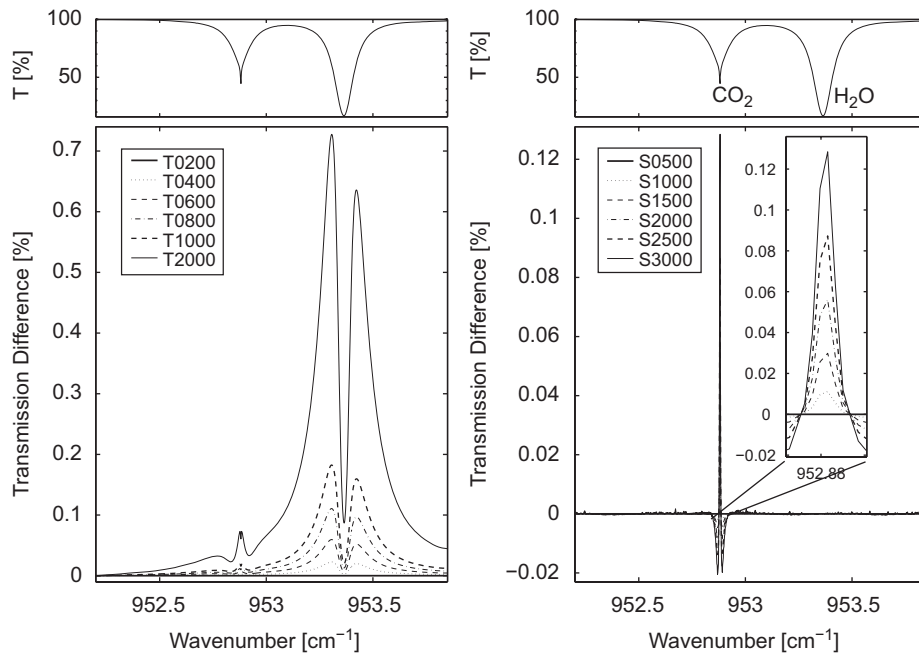


Fig. 6. As in Fig. 5 except for the 953.4 cm^{-1} H_2O microwindow ($E'' = 1962.5\text{ cm}^{-1}$).

transmission difference in the line wings, which is the opposite of what is observed in Fig. 5. The other possibility to explain the calculated transmission differences is via differences in the temperature and pressure profiles, and the subsequent changes in spectroscopic parameters, as per Eqs. (2)–(6). It is more difficult to visualize how the small changes in temperature and pressure in Fig. 2 will translate into transmission differences integrated over the entire atmospheric column, however, there exist two paths for this to happen: (1) via temperature- and pressure-induced changes in the peak of the lineshape function, whose area is normalized to 1 (Eq. (3)), and (2) via temperature-induced changes in the line strength (Eq. (4)).

For the first pathway, we examine the effects of pressure first. Fig. 2 shows a very small systematic effect in the case of the monotonic pressure function whereby the values become larger for more sparse grids, both in the stratosphere and in the troposphere. This occurs because as layer widths increase, the density-weighted pressure that is being plotted as a function of layer midpoint slowly starts to correspond more to a slightly lower height, i.e. the density-weighted height (not discussed up to this point), and, therefore, becomes slightly too high for the layer midpoint. A small increase in pressure will, via Eq. (5), lead to a small increase in the Lorentz broadening coefficient, and a small reduction in the Lorentz line broadening function, which behaves as $f_L(v = v_0) \approx 1/(\pi\gamma_L)$ near line center (see, e.g., [44]). (For H_2O , for heights up to 25–30 km, the Doppler line broadening function is negligible and the Voigt line broadening function is completely dominated by the Lorentz contribution.) Finally, a reduction in f or f_L leads to an increase in transmission, and a positive transmission difference, as defined in our work. It is not completely straightforward to translate the small systematic pressure biases shown in Fig. 2 to quantitative transmission differences, as these will be different for each gas (Eq. (5)) and they will also be a function of height (Eq. (1)). Nonetheless, they will always be positive. In the course of our study we experimented with various grid schemes not shown here; we have observed that the sign of the transmission differences can easily change for a single molecule and microwindow (while the magnitude remains comparable), which in turn indicates that changes in temperature and VMR are more important than the small, albeit systematic pressure biases, which are of the same sign in all cases. Finally, we turn to the effects of temperature in the first pathway. From Eqs. (5) and (6) one can see that, for example, increases in temperature due to misrepresentations of the temperature profile will act in opposite directions to decrease Lorentz broadening on the one hand, and to increase Doppler broadening on the other. For H_2O and other gases primarily found in the troposphere, Lorentz broadening is the overwhelmingly dominant broadening mechanism, leading to net decreases in line width, increases in the peak of the lineshape function

(Eq. (3)), and a decreased transmission. Since it is often found that $0.5 < n_{\text{air}} < 1.0$, similar to the functional exponent of temperature for γ_D , any changes in temperature will tend to compensate at ~ 26 km, where $\gamma_L \sim \gamma_D$, and above (for the species and transitions investigated here, the cross-over height falls on average at 26 km, ranging to as low as 21 km and as high as 32 km). Only in the upper stratosphere, where γ_D is dominant, will an increase in temperature lead to an increase in broadening, a decrease in the peak of the lineshape function, and an increased transmission. This will affect O_3 , NO , and NO_2 the most, since their number concentration profiles peak at or above the cross-over height. Returning to H_2O , we can deduce that the smaller temperatures for grid T2000 between ~ 1 and 3 km (Fig. 2) will lead to a greater broadening, a smaller peak lineshape, and a greater transmission, leading, finally, to positive transmission differences. The opposite will be the case for the higher temperatures for grid T2000 just at or below the tropopause.

The second pathway to affect transmission differences in Fig. 5 is via temperature-induced changes in the line strength. Lower temperatures for grid T2000 between ~ 1 and 3 km will again correspond to a weaker line strength and a higher transmission. Consistent with Fig. 5, this again leads to a positive transmission difference in the line wings, as in the case of the increased broadening parameter discussed above. Conversely, higher temperatures for grid T2000 near the tropopause again lead to negative transmission differences near line center, again consistent with Fig. 5. Since temperature causes transmission differences of the same sign for changes in S as well as in f (via γ_L), we calculated the relative sensitivity of each to a 1-K temperature perturbation. (As stated earlier, the Voigt lineshape function for H_2O tends to $f_L(v = v_0) \approx 1/(\pi\gamma_L)$, thus a consideration of relative changes in γ_L versus S is sufficient.) At 2.5 km, a 1-K increase in temperature leads to a 0.22% decrease in γ_L and a 0.51% increase in S . At 10 km, the relative changes are 0.26% and 0.89% for γ_L and S , respectively. Thus, at 2.5 km the relative sensitivity of line strength to temperature is more than twice as big as the relative sensitivity of line broadening to temperature, increasing to more than three times as much at 10 km. It is important to keep in mind that the overall change in transmission at the central frequency v_0 must also include changes to the VMR profile, and integrate over all layers (Eq. (1)).

In the preceding paragraphs we have outlined, qualitatively, the response of the transmission differences to interpolation errors in temperature and VMR profiles, via broadening and line strength parameters. We also argued that the small systematic pressure biases of Fig. 2 do not drive the transmission differences. Here, we briefly explore the sensitivity of the above functional relationships to the values of the spectroscopic constants themselves, using as an example two separate H_2O transitions. We simulated transmission spectra in another water microwindow (953.3674 cm^{-1}) that has a much larger lower state energy ($E'' = 1962.5 \text{ cm}^{-1}$), giving it a much greater temperature sensitivity (Fig. 7). As expected, Fig. 6 reveals greater transmission differences, which are again positive for highly pressure-broadened regions and negative in the line core (note change in x -axis compression). Since in both microwindows the temperature, pressure, and *a priori* VMR profiles will all have been affected in the same way by interpolation to different grid schemes, the differences in transmission response are only due to differences in the spectroscopic constants found in the HITRAN 2004 database. In Fig. 7 we examine the absolute and relative line strengths of the low and high E'' H_2O and of the interfering CO_2 absorption as a function of temperature. The line intensities were calculated using HITRAN 2004 constants and tabulated partition sums [45]. Vertical lines in Fig. 7 indicate the mean temperature range above Toronto that is affected—via height—by the tropospheric (Txxxx) and stratospheric (Sxxxx) grid schemes. As expected, the lower E'' H_2O absorption feature has a much weaker temperature dependence. Moreover, from the absolute line strength plot we can see that it is weaker in relation to the higher E'' absorption for the lowermost part of the troposphere, where the H_2O VMR profile peaks (Fig. 1). Both factors are consistent with greater transmission differences for grid T2000 in the high E'' microwindow. At 0.728%, these would be detectable (at a 2:1 level) in spectra recorded with an SNR of only 275. We note also that not only is the transmission difference more than twice the value for the low E'' transition, but the net distribution of this difference with respect to the line center has also changed, c.f. Figs. 5 and 6. In particular, the center of Fig. 6 is no longer negative, which is a result of the decreasing importance of transmission differences originating from temperature interpolation errors around 9–12 km, where the line strength decreases drastically for the high E'' transition (Fig. 7).

As expected, the relative importance of broadening versus line strength parameters in driving the changes to $k(\bar{\nu})$ (Eq. (2)) has also changed. For the high E'' transition, we calculated that a 1-K increase in temperature leads to a change in S of 3.32% at 2.5 km and 4.96% at 10 km, compared to changes of only 0.14% and 0.17%

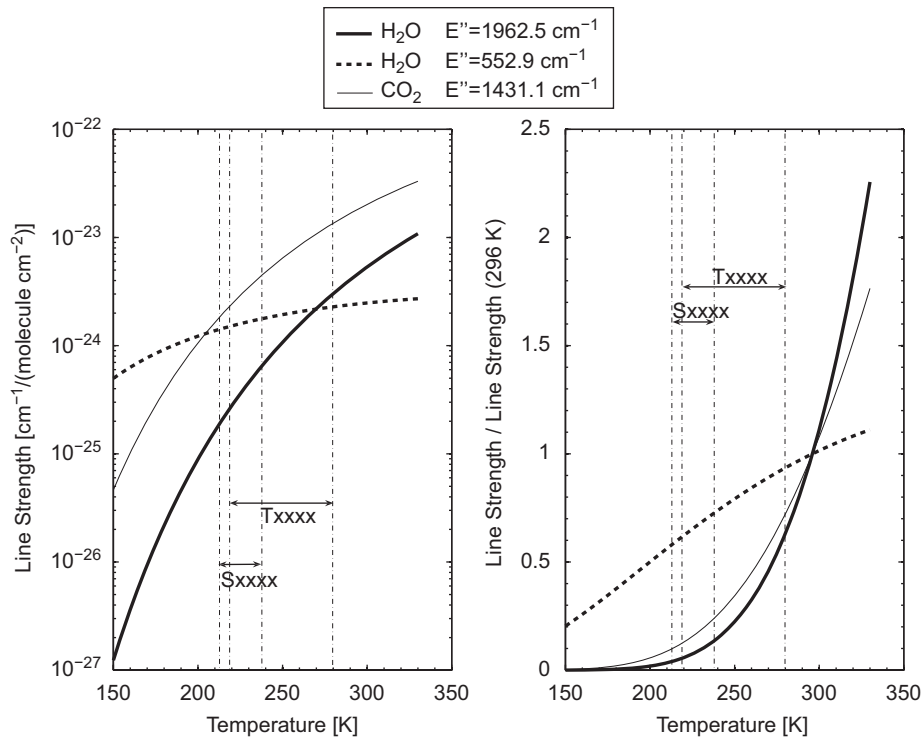


Fig. 7. Absolute (left) and relative (right) line strengths for H₂O absorption features in Figs. 5 and 6, as well as CO₂ in Fig. 6. The dash-dot vertical lines show the mean temperature range above Toronto that is affected—via height—by the tropospheric (Txxxx) and stratospheric (Sxxxx) grid schemes.

in γ_L , respectively, at the same heights. Therefore, in this case, the calculated transmission differences can be more clearly attributed to temperature-induced changes in the line strength, which are ~ 25 times bigger than those in γ_L . As already discussed for the low E'' transition, the misrepresentations of the VMR profile at 2.5 km are very small and they would lead to a transmission difference of an opposite sign. While the VMR profile interpolation errors are much bigger at 10 km, the number concentration profile of water is very strongly attenuated in this region. Therefore, in this case, line strength effects seem to be dominant over both broadening parameters *and* perturbations to the VMR profile.

In Fig. 8 we explore the sensitivity of the tropospheric transmission differences for the high E'' H₂O microwindow to different spectroscopic constants, now changed one at a time. While panel A (similar to Figs. 4 and 6) shows the control transmission differences, panels B, C, and D show how they are altered when various constants are changed with respect to the control. In panel B we simulated the spectra by substituting a lower state energy of $E'' = 552.9 \text{ cm}^{-1}$ instead of $E'' = 1962.5 \text{ cm}^{-1}$. This produced the most marked reduction in the average transmission differences and in their 1σ spread, changing both to more closely resemble the transmission differences of Fig. 5. In panel C we increased the exponent of the temperature dependence of the Lorentz broadening coefficient from 0.39 to 0.59 (the HITRAN 2004 value for the low E'' transition), with very little effect. Finally, in panel D we changed the air- and self-broadening coefficients of the Lorentz broadening function from $\gamma_{\text{air}} = 0.0405$ and $\gamma_{\text{self}} = 0.2360$ to $\gamma_{\text{air}} = 0.0796$ and $\gamma_{\text{self}} = 0.3440$ (the values listed in HITRAN 2004 for the low E'' transition). Compared to the control, the transmission differences in the near wings of the line became broader and of smaller average value, which is consistent with having increased both broadening coefficients and with Eq. (3). The 1σ spread was not changed markedly, confirming that this is driven by the temperature-dependence of the line strength. Finally, the change in average transmission at line center is much smaller for changes in γ than for changes in S , consistent with our calculations of the relative response of each parameter to a 1-K temperature perturbation. Fig. 8 hints at the much greater importance of S as compared to n_{air} , and of the non-negligible effect of γ_{air} and γ_{self} , especially

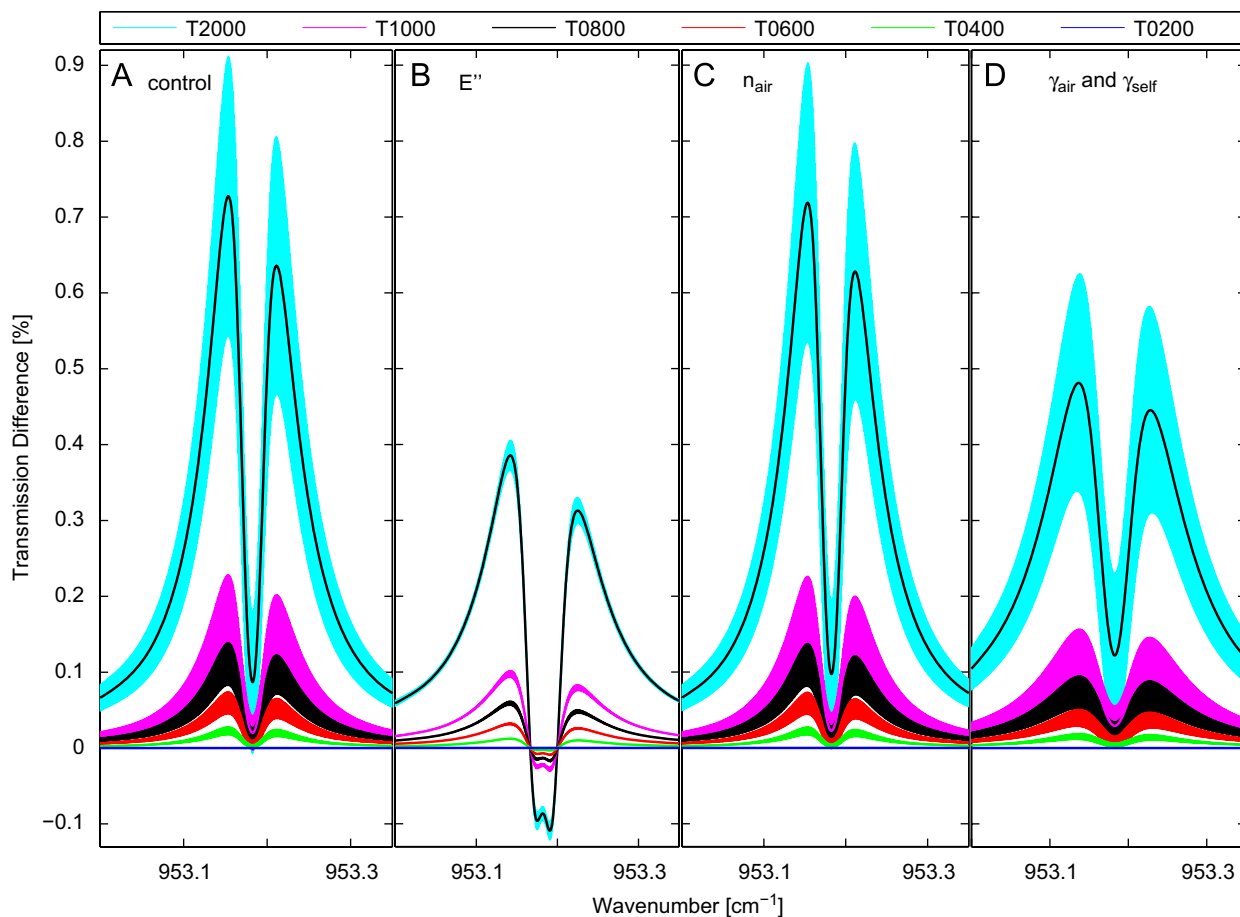


Fig. 8. Transmission differences for the high E'' H_2O absorption in Fig. 4 (Panel A), also showing what happens when certain spectroscopic constants are in turn changed one at a time (panels B, C, and D) to values that correspond to the low E'' transition in Fig. 5. See text for details.

away from line center. However, such a statement is only valid insofar as the range of spectroscopic constants explored in Fig. 8 spans the range of spectroscopic constants found in the HITRAN database. We examined the range of E'' , n_{air} , γ_{air} , and γ_{self} between 940 and 960 cm^{-1} and we conclude that the perturbations to spectroscopic constants illustrated in Fig. 8 are significant for E'' and γ_{air} , becoming a little less so for γ_{self} and n_{air} . In particular, n_{air} tends to high values (e.g. 1.5 or 2) for heavy molecules such as N_2O_5 , SF_6 , or chlorofluorocarbons, which are not a part of our study. In summary, considering Figs. 5 and 6, as well as Fig. 8, it is clear that spectroscopic constants can greatly amplify the response of a given transition to small errors in the temperature and VMR profiles, in turn introduced by interpolation errors when using different grid schemes.

We now turn to the effect of stratospheric grid variations on transmission. In Fig. 6, stratospheric grid variations between 12 and 36 km lead to extremely small average transmission differences ($<0.001\%$) that are not distinguishable from one another near the H_2O line center, as was the case for the low E'' H_2O feature. However, a very sharp transmission difference due to an interfering absorption by CO_2 reaches $\sim 0.129\%$, which would be detectable according to our criteria in measurements with $\text{SNR} = 1550$. The CO_2 response to stratospheric grid differences is not unreasonable given its relatively high VMR in this region (Fig. 1), however, it is not obvious why that narrow response is more than twice as big as the much more pressure-broadened response to tropospheric grid differences, where $\sim 90\%$ of the total column of CO_2 resides. Fig. 7 shows that this CO_2 feature is also highly sensitive to temperature, however, that is less true for stratospheric temperatures, where the absolute line strength is much reduced anyway. From Fig. 2 we can see that the

temperature errors are about twice as big in the region from 16 to 22 km than at 2.5 km, which may be a compensating factor. Other factors may also be at play, such as small gradients in our CO₂ *a priori* VMR profile in the stratosphere but not in the troposphere, and the larger extent of the altered stratospheric region as compared to the altered tropospheric region. Moreover, Doppler broadening becomes as important as Lorentz broadening only at 32 km. Finally, although of limited practical interest, we note that the pressure-broadened CO₂ transmission difference due to tropospheric grid changes shows a small dip in the very center of the line, which is consistent with temperature and VMR profile changes (the latter not shown for CO₂) in the low-pressure 9–12 km region (Fig. 2).

3.2. Implications for maximum tropospheric layer width

Table 3 summarizes the measurement SNR needed such that the highest systematic transmission differences near line center would still be twice as big as the noise for all the trace gases and transitions we examined as part of our study. In order to draw conclusions about the maximum layer width necessary to faithfully represent the transmission of any gas, not just H₂O, we must put these values in a wider context. The SNR used in retrievals from TAO spectra is ~ 500 on average, hence the values given in Table 3 may seem unattainable, except for H₂O, CO, O₃, ClONO₂, and HF. However, it is important to note that the SNR of ~ 500 is calculated from the RMS residuals of typical spectral fits (following common practice in the IRWG), which include both random and systematic fitting errors. If the SNR is calculated (more conventionally) as signal in the spectrum divided by noise in a nearby saturated region, then one obtains, on average, values of ~ 1000 from TAO spectra. This number can easily be doubled at IRWG stations where the influence of water vapor on baseline signal levels is smaller, e.g. at polar or mountain stations. However one must keep in mind that the smaller *a priori* VMR profile of H₂O would also make the transmission differences smaller, while greater SZAs often used in the observations from such sites can serve to again increase them. Nonetheless, improvements in the SNR achievable in Toronto are realistic given present and future improvements to instrumentation, signal acquisition and signal processing, and for this reason we assume 2000 as the maximum achievable SNR, which then makes transmission differences of $> 0.1\%$ twice as big as the measurement noise. Accordingly, we are led to conclude that the tropospheric grid spacing of 2 km causes detectable systematic transmission differences for H₂O, as well as for CO, ClONO₂, and HF (also via H₂O interferences). The stratospheric grid spacing of 3 km leads to detectable systematic transmission differences for CO₂, N₂O, CO (via O₃ interferences), O₃, ClONO₂ (again, via O₃), HCl, and HF. It is interesting to note that stratospheric species can be affected by tropospheric grid spacing [34] and vice versa, i.e. the interferences of O₃ and N₂O in the CO microwindows.

In the following sections we show transmission difference spectra for all species, regardless of the values presented in Table 3. Using this information and knowledge of typical SNRs due to *random* spectral noise, other investigators can draw their own conclusions as to the maximum layer width they should use in the troposphere and stratosphere in their retrievals.

To answer the question of what should be the *maximum* tropospheric layer width, we focus on H₂O, which will be shown to cause all the significant tropospheric transmission differences either directly, or as an

Table 3

Approximate SNR required to detect the largest average transmission SNR differences either due to target or interfering species (in brackets) in Figs. 5, 6, and 9–22 at a 2:1 level (see text for details)

	H ₂ O _{loE}	H ₂ O _{hiE}	CO ₂	CH ₄	N ₂ O	CO _{Tr}	CO _{St}	N ₂
T2000	662	275(4000)	4000	4556	2500	5988 (1515)	5000 (1575)	5917
S3000	–	– (1550)	1550	4301	1653	– (2130)	7547 (478)	3279
	O ₃ F ₆	O ₃ F ₃	NO	NO ₂	HNO ₃	ClONO ₂	HCl	HF
T2000	–	–	– (3610)	–	– (7874)	– (238)	–	– (194)
S3000	595	2051	9756	–	7633	– (648)	1129	1156

Only the case of differences due to the most sparse tropospheric (T2000) and stratospheric (S3000) grids is shown, and “–” indicates values $> 10^4$.

interfering species in another microwindow. We examine the intermediate grid schemes to determine the layer width that just starts to produce significant, i.e. $>0.1\%$ transmission differences ($\text{SNR} < 2000$). When designing the grid spacings given in Table 2 we began with a layer width of 0.2 km (T0200) between 0 and 12 km in order to match the spacing used internally by FSCATM. We used a maximum width of 2 km, as per previous work summarized in Table 1, but focused on widths of between 200 m and 1 km. For the low E'' H_2O transition (Fig. 5) all the tropospheric layer widths of 1 km or less lead to transmission differences of less than 0.1%, suggesting that a width somewhere between 1 and 2 km would suffice. For the high E'' H_2O transition (Fig. 6) the tropospheric layer width of 0.8 km just crosses our threshold of detection, implying that this should be the maximum layer width. Water is a trace gas found in abundance in the atmosphere, although its VMR profile is highly variable depending on location and season. As mentioned previously, it leads to significant transmission differences as an interfering species in microwindows used for the retrieval of CO (Figs. 12 and 13), ClONO_2 (Fig. 20), and HF (Fig. 22). While we discuss these in more detail below, based on the large H_2O interference in the HF microwindow ($E'' = 1631$ and 2225 cm^{-1} also nearby), a maximum tropospheric layer width of 0.6 km is recommended. In practice, it is likely that such a spacing is most necessary only near the surface, where the number concentration profile of H_2O peaks. Subsequently, the layer width may be gradually increased with increasing altitude until the maximum stratospheric width is reached (Section 3.7).

3.3. Transmission differences of N_2

In the remaining subsections, we examine—in much less detail—the transmission difference plots of a series of other trace gases that are regularly retrieved and reported by NDACC members. The only exception is N_2 , which is a species not reported but instead used diagnostically due to the fact that its VMR profile is well known and constant. Our N_2 *a priori* profile (not shown in Fig. 1) is simply 0.781 at all heights. Since there can be no errors due to VMR profile interpolation, any transmission differences must be due to temperature. (As explained in Section 3.1, we have deduced that the small and systematic pressure differences shown in Fig. 2 are not what is driving the transmission differences.) Fig. 9 shows the calculated transmission differences in response to tropospheric and stratospheric grid changes, as outlined in Table 2. Near line center, these are 0.034% and 0.061%, respectively, and would require a measurement SNR of ~ 5900 and ~ 3300 so as to be twice as large as the noise. These values are much greater than our 2000 threshold, making the N_2 transmission differences insignificant, for any tropospheric or stratospheric layer width. We note some general features of the plot, which are that, as expected tropospheric grid changes produce more broadened transmission differences than stratospheric grid changes; furthermore, as in the case of the CO_2 interference in Fig. 6, stratospheric grid changes lead to transmission differences that are nearly twice the magnitude of those due to tropospheric grid changes. Unlike CO_2 , N_2 has a constant VMR profile, and the strength of the pressure-induced dipole transition of N_2 is nearly independent of temperature for all atmospheric temperatures. Therefore, the transmission differences must be produced primarily via increases or decreases in γ_L and γ_D . A closer inspection of the shape of the stratospheric transmission differences shows that they are in fact composed of a broader negative contribution and a narrower positive contribution. These are consistent with increases in temperature around 16–22 km leading to a reduced γ_L , and slight decreases in temperature between 22 and 36 km (visible with magnification in Fig. 2) leading to an increased γ_D , perhaps also in combination with a very slight increase in the transition line strength ($< 5\%$) toward lower temperatures. (We calculate the $\gamma_L \sim \gamma_D$ cross-over height for N_2 as 22 km.) For other molecules, where gradients in the VMR profile and a temperature-dependence of S are observed simultaneously with temperature interpolation errors, this reasoning cannot be expected to hold.

3.4. Transmission differences of CH_4 , N_2O , and CO

Figs. 10 and 11 show the transmission difference plots for CH_4 and N_2O . The plots again show broader features for tropospheric grid changes and narrower features for stratospheric grid changes. While changes for CH_4 are negligible for all grids, N_2O shows some sensitivity to the stratospheric grid spacing. Moreover, while the response of CH_4 in both panels is of very similar magnitude, the response of N_2O is greater for

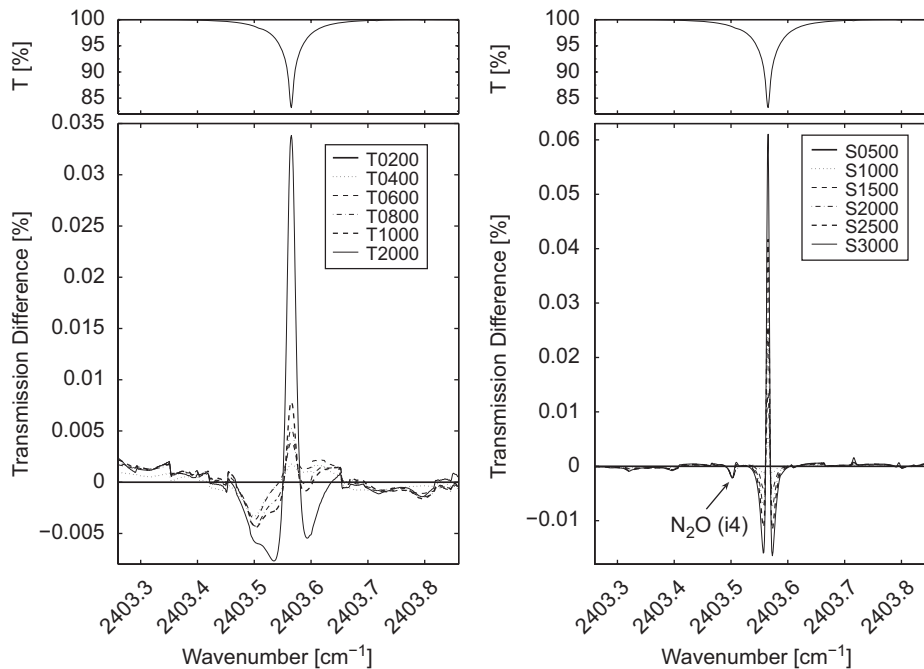


Fig. 9. As in Fig. 5 except for the N_2O microwindow.

stratospheric grid changes, as was the case for CO_2 and N_2 . As before, these responses could be explained by a combination of the temperature errors introduced by interpolation to different grids, similar errors produced in the VMR profile, the temperature sensitivity of the transition line strength, and, finally, the temperature sensitivity of the broadening parameters, with their subsequent effect on the peak magnitude of the lineshape function. Since the transmission differences are not significant, we will forego this exercise and only note that the line strength of this N_2O transition is virtually independent of temperature, while that of CH_4 increases by approximately 60% around 16–22 km. Furthermore, while N_2O is well-mixed in the troposphere but has more of a gradient in the stratosphere, our *a priori* VMR profile of CH_4 increases significantly toward the surface and has relatively less of a gradient in the stratosphere. Finally, the Lorentz-to-Doppler cross-over height is 26 km for N_2O and 22 km for CH_4 .

Fig. 12 shows annual average transmission differences for CO in the saturated 2158.2997 cm^{-1} region, while Fig. 13 shows the weakly absorbing ^{13}CO region at 2117.4307 cm^{-1} . The two absorption features were used in this study because they have been shown to be sensitive to CO in the troposphere and stratosphere, respectively [44], they have similar lower state energies ($E'' = 23.1$ and 55.1 cm^{-1}) and their Lorentz-to-Doppler cross-over heights are also similar (~ 25 km). The interfering absorptions in the “stratospheric” microwindow are all due to O_3 , with the exception of one feature at 2117.15 cm^{-1} that blends O_3 and CO_2 absorptions. The baseline transmission difference increasing toward lower wavenumbers in Fig. 13 is due to the wing of a nearby H_2O absorption. Both microwindows exhibit significant transmission differences due to changes in the tropospheric grid spacing, however, these are due to interferences from H_2O . As summarized in Table 3, SNRs of more than 5000–6000 would be needed to detect the transmission changes due to CO itself, while SNRs of only 1500–1600 would make those due to H_2O visible. Also interesting are the responses of these two microwindows to changes in the stratospheric grid spacing, which are bigger for interfering species than for CO itself. The right panel of Fig. 12 shows transmission differences due to two interfering N_2O features (qualitatively similar to the response of N_2O in Fig. 11), while the right panel of Fig. 13 is completely dominated by transmission differences due to the ubiquitous transitions of O_3 . Although there are over 100 O_3 transitions in this microwindow, those with the highest lower state energies ($\sim 2000\text{ cm}^{-1}$) are negligibly weak; nevertheless, there are many strong transitions displaying significant temperature dependence. At up to 0.42%, these transmission differences constitute the strongest response to stratospheric grid changes in a

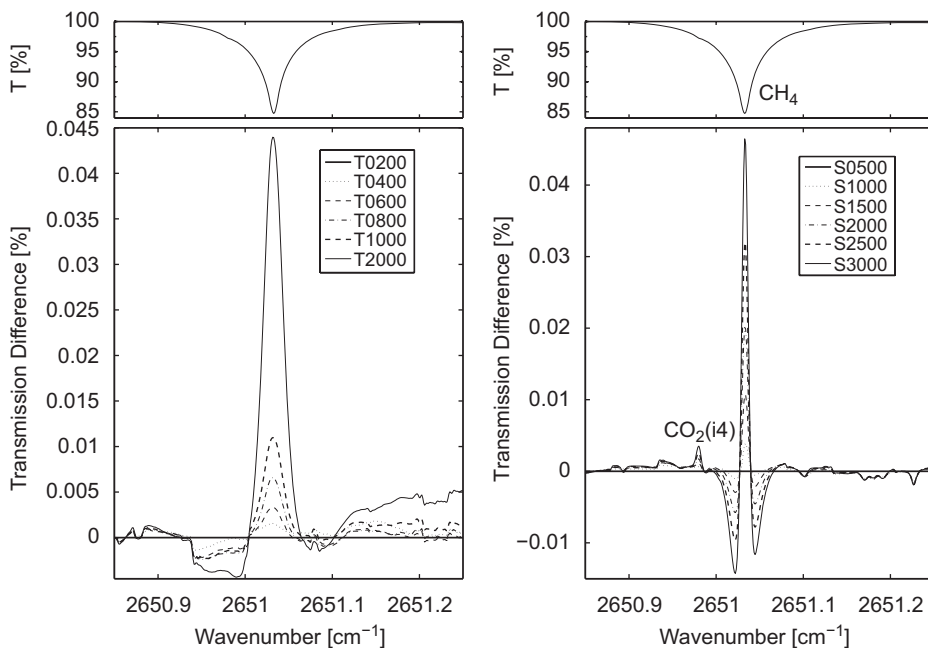


Fig. 10. As in Fig. 5 except for the CH₄ microwindow.

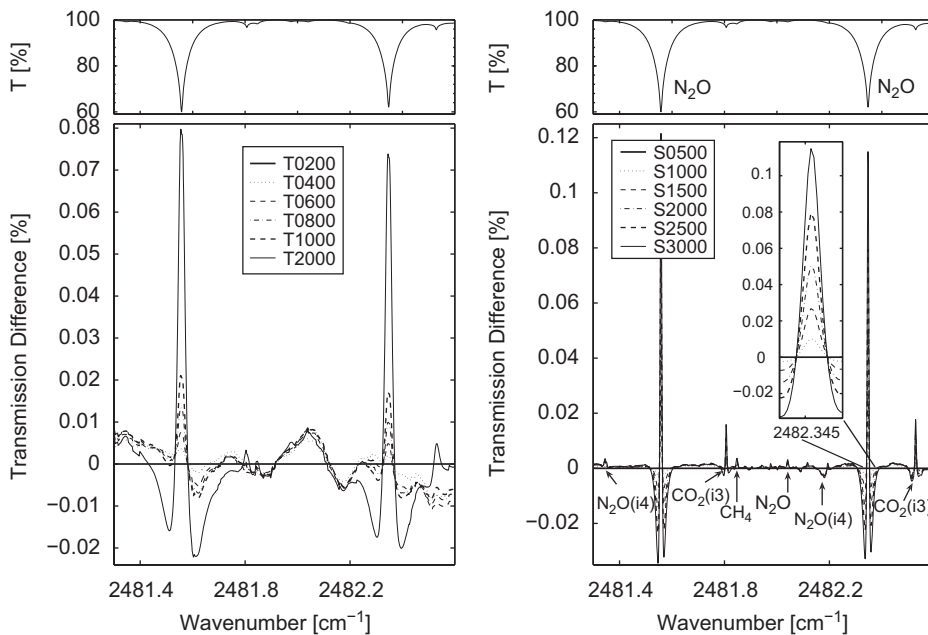


Fig. 11. As in Fig. 5 except for the N₂O microwindow.

microwindow used to retrieve a tropospheric gas. We will discuss grid spacings appropriate for O₃ in Section 3.5.

The fine details of the shape of the transmission difference response for CO will be due to a mixture of both temperature and VMR profile interpolation errors. Strong CO gradients are present in all regions of the

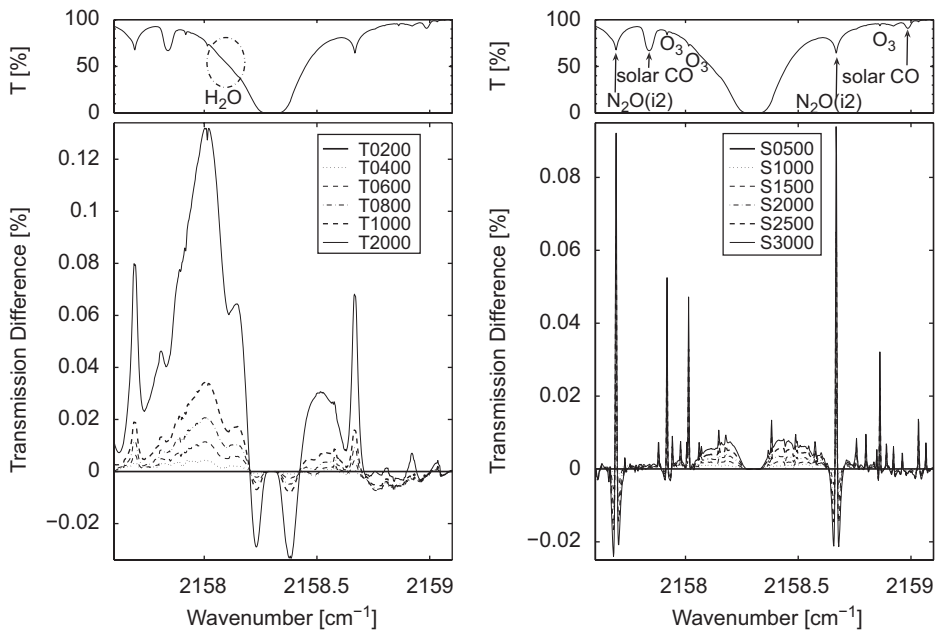


Fig. 12. As in Fig. 5 except for the CO microwindow sensitive to the troposphere.

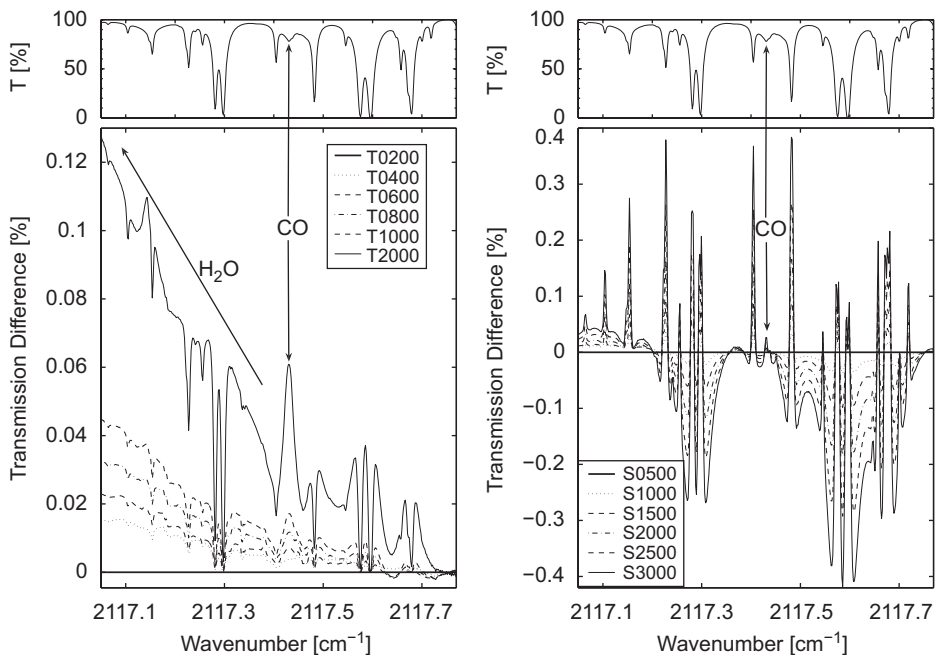


Fig. 13. As in Fig. 5 except for the CO microwindow sensitive to the stratosphere.

atmosphere, but interpolation errors in those nearest to the surface will have the greatest influence on transmission. Finally, both CO transitions display a very similar sensitivity to temperature, which is intermediate between that of N_2 or N_2O and CH_4 , with both CO line strengths increasing by $\sim 35\%$ around 16–22 km.

3.5. Transmission differences of O_3

Figs. 14 and 15 show annual average transmission differences for the isolated O_3 absorption at 1146.4714 cm^{-1} and for the multiple O_3 absorptions in the 3045 cm^{-1} microwindow, respectively. As expected, the maximum tropospheric transmission difference in both microwindows is negligibly small at $<0.01\%$ (Table 3). The 1146 cm^{-1} microwindow gives an example of extremely small annual average tropospheric transmission differences that are in fact well separated from one another for the different grid spacings (see inset in Fig. 4). This is not the case in the 3045 cm^{-1} microwindow, where the broad pattern of transmission differences does not come from the O_3 transitions, but instead from the wing of a nearby CH_4 feature that is recognizable only as the baseline transmission decreasing toward higher wavenumbers.

In response to stratospheric grid variations, the 1146 cm^{-1} region shows transmission differences that are more than three times as large as those in the 3045 cm^{-1} region. The former reach 0.34% while the latter fall just below our detection criterion of 0.1% , requiring SNRs of 595 and 2051, respectively, for detection (Table 3). After an examination of the temperature dependence of the different O_3 transitions in both microwindows, we can conclude that the dominant factor for the calculated transmission differences is the misrepresentation of the *a priori* VMR profile of O_3 on the coarser stratospheric grid, as shown in Fig. 16. This can be deduced as follows. First of all, for the 1146 cm^{-1} region we calculated that the relative change in S at around $16\text{--}22\text{ km}$ in response to a 1-K temperature perturbation is of very similar magnitude ($\sim 0.35\%$) and opposite sign as the relative change in f_L (the Lorentz-to-Doppler cross-over height for this transition occurs at 31 km). This implies that the two effects would tend to cancel each other out. Second, in the 3045 cm^{-1} region ($\gamma_L \sim \gamma_D$ at 26 km) relative changes in S can be twice the magnitude of those in f_L , however, the line strengths in this microwindow display both positive and negative temperature dependencies. If the temperature dependence of S was the dominant effect, then the transmission differences should be both positive and negative to reflect this. (The sign of the transmission difference in the 1146 cm^{-1} region is opposite to what would be expected given the fact that this transition's strength decreases with decreasing temperatures.) Finally, the only remaining factor that can be responsible for the transmission differences in Figs. 14 and 15 is the change in the O_3 profile shown in Fig. 16. It is in fact consistent, as follows: smaller number concentrations of O_3 for grid S3000 near the peak at $\sim 22\text{ km}$ will produce greater transmissions and a positive transmission difference with respect to grid S0500; very slightly greater number concentrations of O_3 for grid S3000 in the segment between

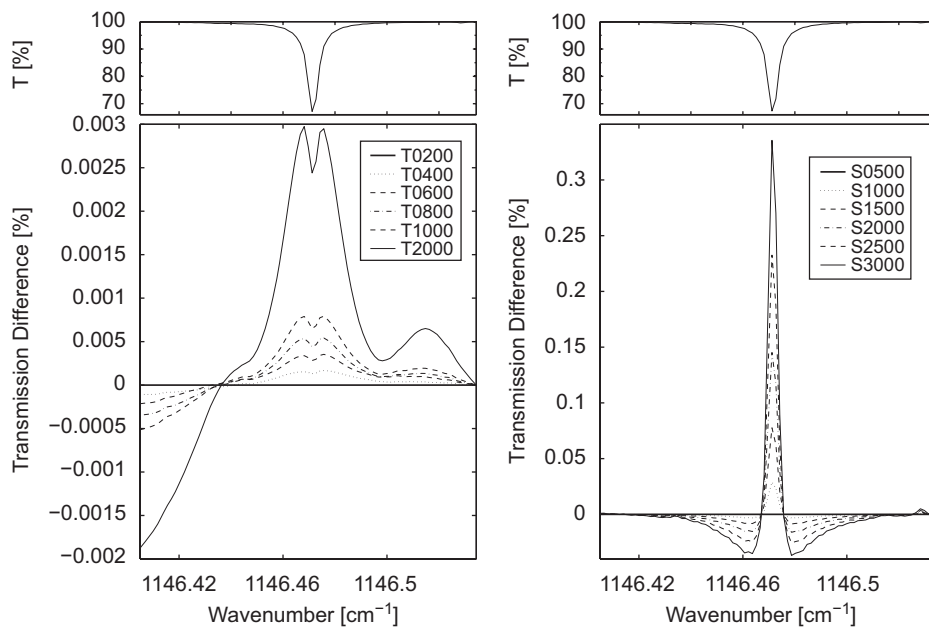


Fig. 14. As in Fig. 5 except for the 1146 cm^{-1} O_3 microwindow.

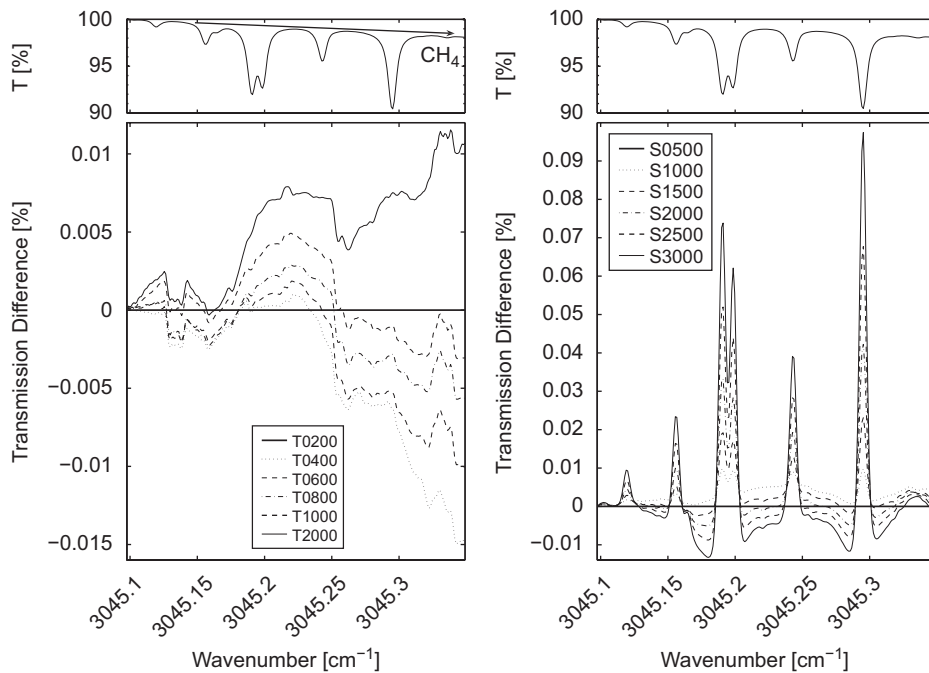


Fig. 15. As in Fig. 5 except for the 3045 cm^{-1} O_3 microwindow.

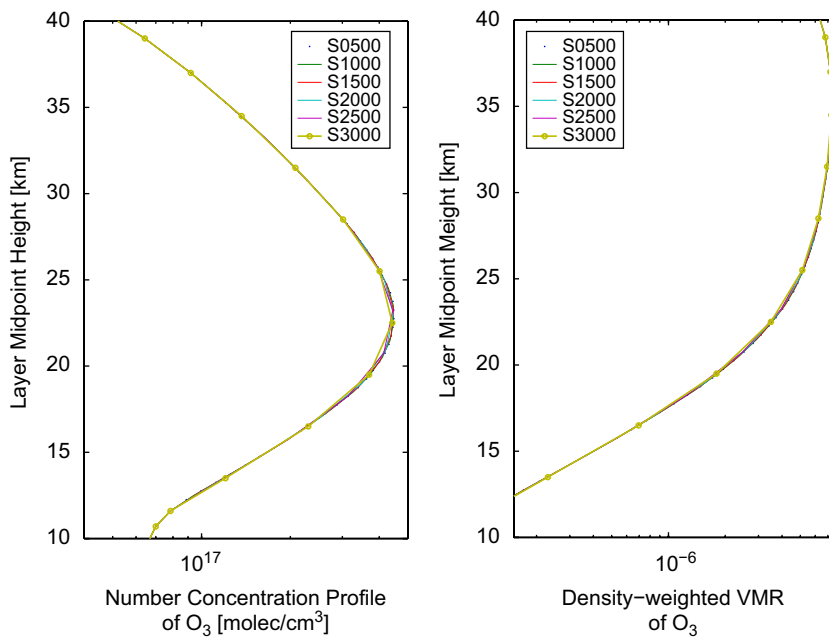


Fig. 16. Mean number concentration (left) and density-weighted VMR (right) profile of O_3 above Toronto calculated on differently spaced stratospheric grids.

12 and 20 km will lead to weaker transmissions and a (much smaller) and more pressure-broadened negative transmission difference, as found in both the 1146 and 3045 cm^{-1} regions. The fact that the number concentration profile of O_3 already exhibits very little to no changes for the different grid schemes above

~28 km (whereas the grids are different up to 36 km) implies that any grid changes above 36 km will have negligible effects on the transmission of O₃. The implications for maximum stratospheric layer width will be discussed in Section 3.7, after we have examined O₃ as an interfering species in the ClONO₂ microwindow, as well as the effects of stratospheric grid changes on HCl and HF in Section 3.6.

3.6. Transmission differences of selected stratospheric gases

Figs. 17 and 18 show annual average transmission differences for NO and NO₂ in the commonly used 1900.08 and 2914.65 cm⁻¹ absorbing regions, respectively. The response of both regions to tropospheric grid changes, while negligible, seems primarily via broad interfering CO₂, H₂O, and CH₄ absorptions. The annual average transmission differences due to tropospheric grid changes are not clearly separated for either molecule, unlike the case in Fig. 4; in the stratospheric panels, only the annual mean transmission differences due to NO (and the nearby sharp CO₂ interference) are distinguishable from one another in this sense. As expected, the strong absorption due to CO in Sun's gaseous exterior (Fig. 17) does not respond to any changes in the discretization of Earth's atmosphere, although the transmission difference is not quite zero due to neighboring gases. Regardless of which combination of interpolation errors and temperature sensitivities plays what role, none of the transmission differences in either the troposphere or the stratosphere are significant according to our 2000 SNR (or 0.1% transmission difference) criterion.

Fig. 19 shows annual average transmission differences for HNO₃ in the commonly used broad absorbing region near 868 cm⁻¹. Although they are of a comparable magnitude, HNO₃ transmission differences due to both tropospheric and stratospheric layer width changes are negligible (Table 3); furthermore, it is clear that the dominant tropospheric effects are caused by a nearby H₂O transition, while stratospheric effects are clearly due to the complex HNO₃ spectroscopy itself. There is some indication of a superposition of highly pressure-broadened tropospheric transmission differences due to HNO₃ itself, which would be consistent with the significant increase in its *a priori* profile near Toronto's urban surface (Fig. 1). Finally, small as they are, upon closer inspection (not shown) the transmission differences are all very well separated from one another, even in the case of the highly structured responses to stratospheric grid changes.

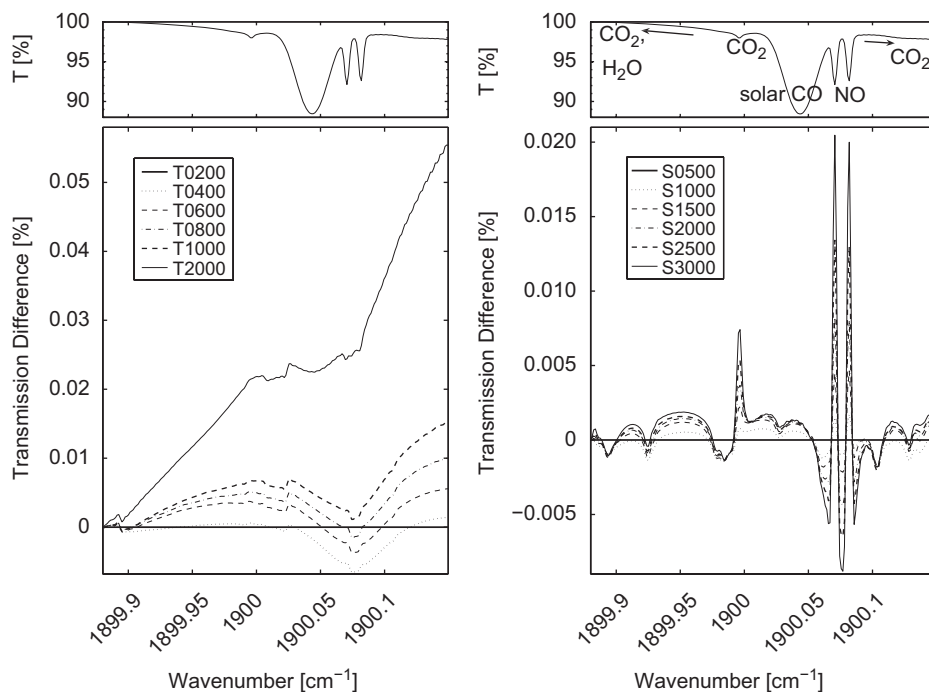


Fig. 17. As in Fig. 5 except for the NO microwindow.

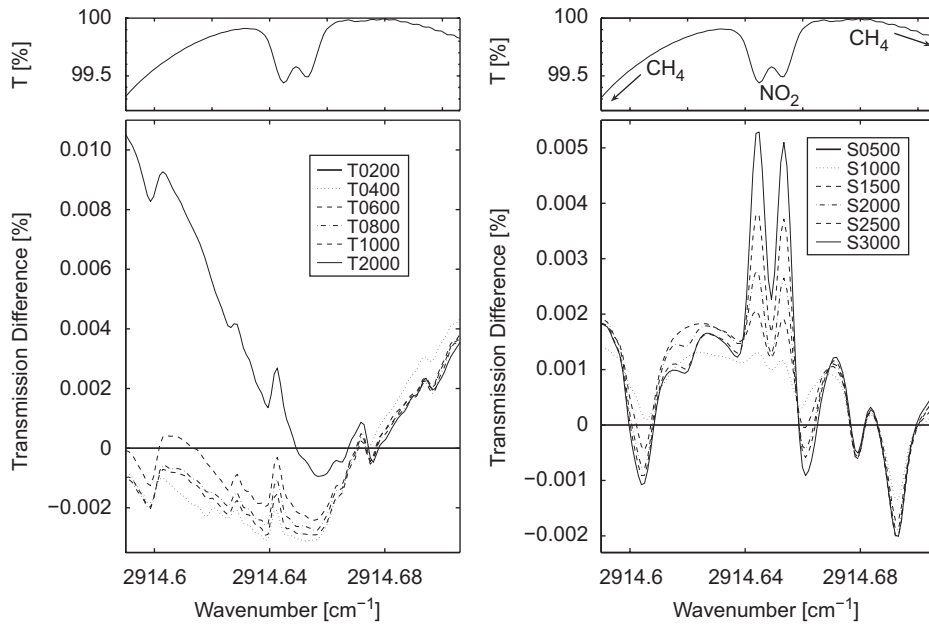


Fig. 18. As in Fig. 5 except for the NO_2 microwindow.

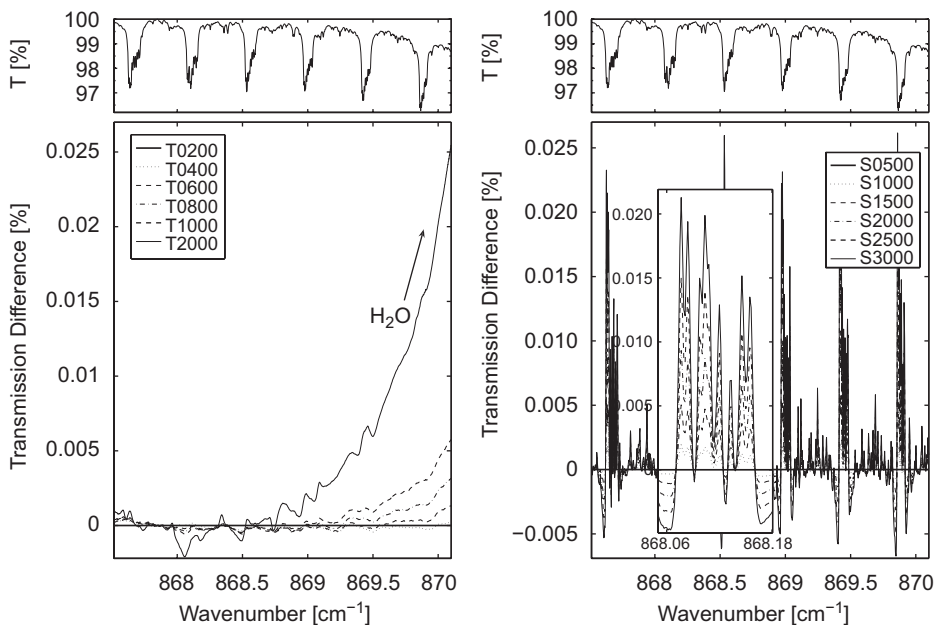


Fig. 19. As in Fig. 5 except for the HNO_3 microwindow.

Fig. 20 shows annual average transmission differences for ClONO_2 in the microwindow including its Q-branch at 780.22 cm^{-1} . This broad microwindow has been used in a two-step approach to retrieve ClONO_2 , whereby interfering species such as H_2O , CO_2 , and O_3 are retrieved first, while ClONO_2 is found in a second pass at the problem and using a more focused spectral region [46]. The tropospheric response of the broad ClONO_2 microwindow is dominated by the temperature-dependent ($E'' = 1475 \text{ cm}^{-1}$) and saturated H_2O transition; it is similar in magnitude and in its 1σ spread (not shown) to the response of H_2O in Fig. 6.

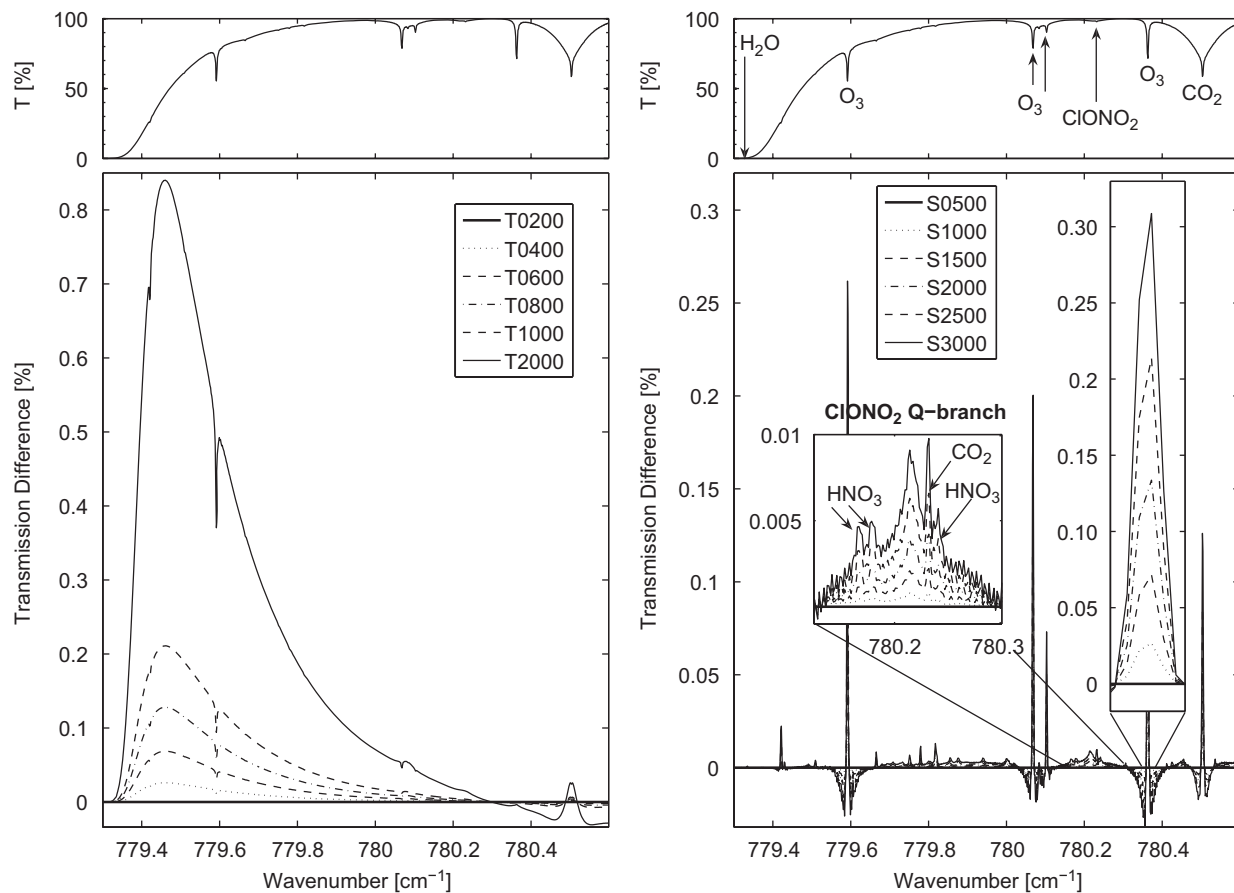


Fig. 20. As in Fig. 5 except for the broad ClONO_2 microwindow.

The response to stratospheric grid changes is weak for ClONO_2 itself (see inset), but strong and significant for the interfering O_3 and CO_2 transitions. All stratospheric transmission differences (including the slight response of ClONO_2) are very clearly separated from one another when inspected on a magnified scale (not shown). As in the case of O_3 in Figs. 14 and 15, this response to stratospheric grid changes is caused by interpolation errors in the profile of O_3 near its number concentration peak. The O_3 interferences immediately to the left of the ClONO_2 Q-branch are included in the narrow microwindow analysis approach of Reisinger et al. [46], and the O_3 feature immediately to the right is partially included as well. ClONO_2 is the first example of a stratospheric gas that is strongly affected by tropospheric layer width, especially if the method of analysis of its spectra uses the broad microwindow simulated here. The other such example is HF, discussed below.

Figs. 21 and 22 show annual average transmission differences for HCl and HF in the commonly used 2925.90 and 4038.96 cm^{-1} absorbing regions, respectively. These two lines have a very similar sensitivity to temperature, increasing in strength by $\sim 30\%$ around 16–22 km (with respect to the strength at the warmer temperatures near the surface). The increases in temperature near 16–22 km, e.g. for S3000, would lead to a reduced line strength, an increased transmission, and positive transmission differences, as shown in Figs. 21 and 22. However, these positive transmission differences are also consistent with the coarsest stratospheric grid leading to slight decreases of both HCl and HF number concentration profiles at and below their maximum at ~ 20 km (not shown). Finally, for HCl and HF, the temperature sensitivity of f via the broadening parameters is not at all negligible compared to the temperature sensitivity of S , with Doppler effects becoming important above 21 km for HF and above 25 km for HCl. Next to O_3 , these two gases show the most significant response to stratospheric layer width variations. Tropospheric variations produce clear but

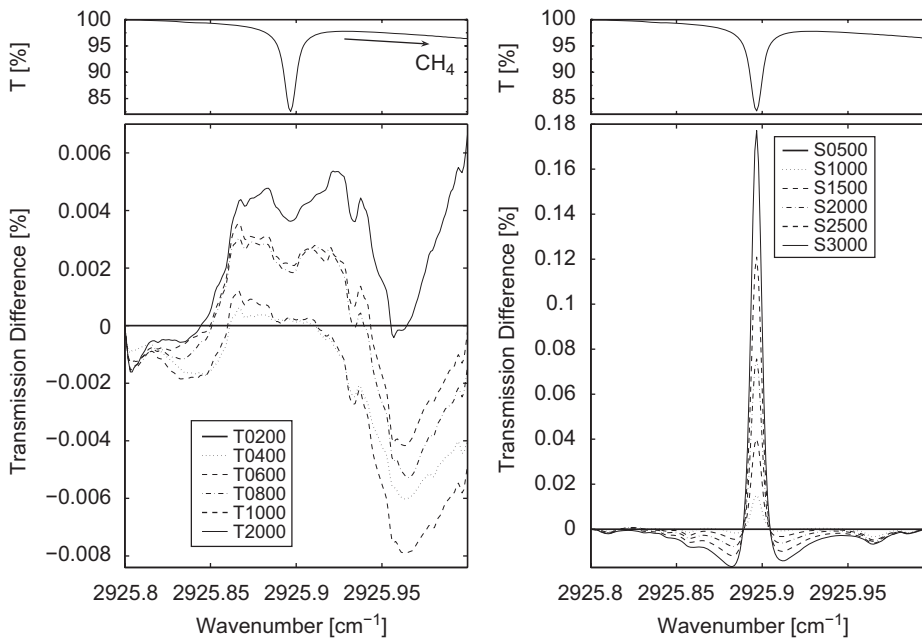


Fig. 21. As in Fig. 5 except for the HCl microwindow.

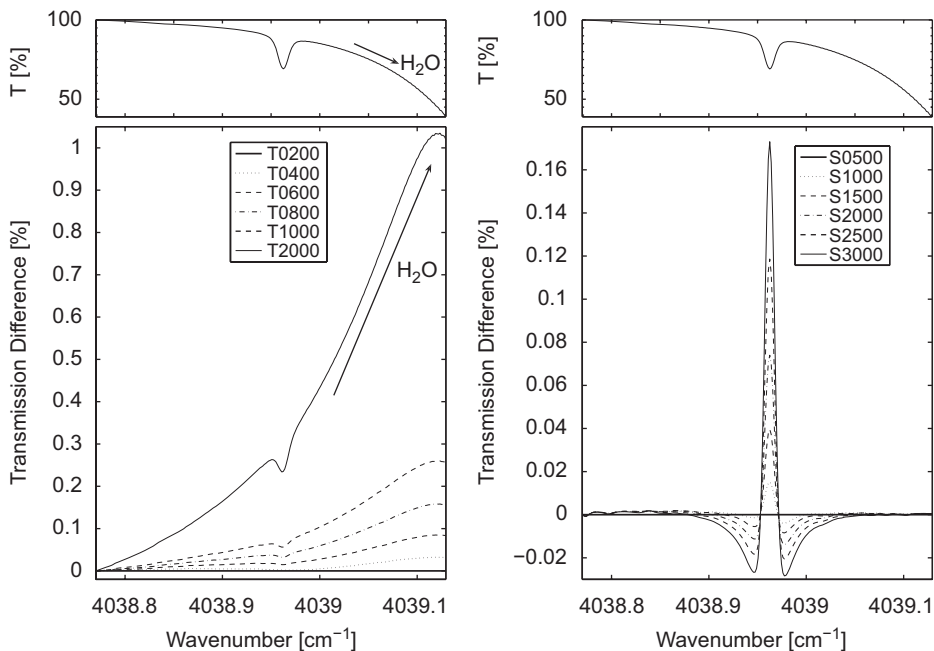


Fig. 22. As in Fig. 5 except for the HF microwindow.

negligible transmission differences in the HCl microwindow due to the wing of a CH₄ absorption. In the HF microwindow, the wings of two highly temperature-sensitive absorptions of H₂O ($E'' = 1631$ and 2225 cm⁻¹) produce the largest transmission differences in the entire study. Greater than 1%, they would appear as twice the noise in spectra recorded with an SNR of only ~ 200 . As discussed in Section 3.2, it is the ubiquitous presence of such highly temperature-sensitive H₂O features that may be viewed as the driving factor for a

maximum tropospheric grid width of 0.6 km. HF is the second example of a stratospheric gas whose transmission spectrum is strongly affected by the tropospheric grid spacing, again, via an H₂O interference.

3.7. Implications for maximum stratospheric layer width

To answer the question of what is the *maximum* permitted stratospheric layer width so that transmission spectra are faithfully represented, we must focus on O₃, which was shown to cause the most significant stratospheric transmission differences either directly, or as an interfering species in another microwindow (CO and ClONO₂). As in the case of H₂O and tropospheric layer widths, we examine the intermediate stratospheric grid schemes to determine the layer width that just starts to produce significant, i.e. >0.1% transmission differences. When examining the transmission plots of HCl and HF in isolation (Figs. 21 and 22), the maximum layer width can be between 2 and 2.5 km. Similarly, in the case of CO₂ and N₂O (Figs. 6 and 11) we may choose the maximum width even closer to 3 km. However, based on the strong O₃ absorption in the 1146 cm⁻¹ region, stratospheric layer widths should be no more than ~2 km. As in the case of H₂O, this recommendation must be qualified. This maximum grid width is most applicable in the region of strongest gradients in the O₃ number concentration profile, which falls between 20 and 25 km (Fig. 16).

4. Summary and conclusions

In this study we assessed the effects of the vertical discretization of the atmosphere on modeled transmission spectra in the mid-infrared range. The FSCATM forward model employed in our calculations is a part of the SFIT-2 algorithm commonly used to retrieve trace gas profiles from high-resolution ground-based solar absorption FTIR spectra; however, our results consider transmission in general and, therefore, have wider applicability to radiative transfer problems of absorption in a near-zenith or near-nadir configuration. In our study, all radiative transfer calculations were performed at a solar zenith angle (SZA) of 45°, and larger transmission differences are to be expected for greater angles.

We modeled transmission spectra using HITRAN 2004 spectroscopic parameters in microwindows typically employed in profile retrievals within the NDACC IRWG, as described in detail in Section 2. We constructed a finely spaced retrieval grid of 0.2 km in the troposphere and 0.5 km in the stratosphere and analyzed transmission differences resulting from progressively making these grid schemes more sparse (up to 2.0 km) in the troposphere, defined as 0–12 km, and in the stratosphere (up to 3.0 km), defined as 12–36 km for the purpose of our study. We did not analyze the effects of grid spacing above 36 km, but we expect them to be small for all gases with possibly the exception of NO.

We compared the magnitude of the transmission differences resulting from different grid schemes to that resulting from the typical variation of temperature and pressure above Toronto over the course of one year. Using 362 NCEP profiles of temperature and pressure, we found that the 1 σ spreads in the annual means of the transmission differences are small enough that the annual means themselves can be considered well separated from one another for all grid schemes. This assumption only breaks down away from the centers of sharp transitions and for NO₂.

We analyzed a suite of molecules, including (in order) H₂O, CO₂, N₂, CH₄, N₂O, CO, O₃, NO, NO₂, HNO₃, ClONO₂, HCl, and HF in microwindows commonly used in FTIR spectroscopy. Some gases (e.g. H₂O, O₃, and CO) were analyzed in multiple microwindows, either as targets, or as interfering species. Systematic differences in modeled transmissions are apparent when coarser grid schemes are used for all species and microwindows, though some are below random noise levels typical of Toronto spectra, which we take to be one part in 2000, at best. The most significant transmission differences occur for H₂O (0.30–0.73%) and O₃ (0.10–0.34%) when coarse tropospheric and stratospheric grids are used, respectively. CO (0.13%), ClONO₂ (0.84%), and HF (1.03%) are also influenced when the tropospheric grid is varied via the interference of H₂O, which is in turn sensitive to temperature interpolation errors via the lower state energy of the particular H₂O transition. (The transmission differences actually due to CO and ClONO₂ transitions themselves are not significant, while those due to HF are.) Next most important after H₂O, O₃ is a significant interference in the CO (0.42%) and ClONO₂ (0.31%) microwindows when the stratospheric grid scheme is made more coarse, however, its influence is felt primarily via interpolation errors in the O₃ number

concentration profile introduced by the coarser grids, not via the temperature profile. Finally, HCl and HF both show a significant response in transmission to coarser stratospheric grids ($\sim 0.18\%$), which may be attributable to both interpolation errors in temperature around 16–22 km, and to decreases of their VMR profiles under a coarser grid scheme.

The transmission errors above are comparable in magnitude to forward model errors introduced by, e.g. using the Voigt lineshape approximation instead of the soft collision model discussed by Barret et al. [35] for HCl and HF. In that study, transmission differences of 0.2% and 0.5% were found for HCl and HF, respectively. It is important to note that systematic forward model errors such as the discretization effects discussed in our study or the line narrowing effects discussed by Barret et al. are much smaller than the quoted errors on transition strength in the HITRAN 2004 database. These are 5–10% for most H₂O and O₃ transitions in the mid-IR. However, while spectroscopy errors are a central issue in transmission modeling, it is valuable and essential to examine the smaller forward model errors in isolation.

We have argued that temperature and VMR profile interpolation errors are more important than the small, albeit systematic, changes in the pressure introduced by a more coarse grid. It is not easy to discern whether it is indeed temperature or the VMR profile that is the dominant factor in altering the transmission difference spectra of any given gas; furthermore, for temperature, it is not always clear if the changes are via the temperature sensitivity of the line strength or via the temperature sensitivity of the Lorentz and Doppler line broadening parameters. In one final complication, the different spectroscopic constants of different quantum mechanical transitions of the same gas can lead to significant changes in transmission difference spectra, as illustrated in detail in the case of H₂O.

Considering only those transmissions $> 0.1\%$ as significant in measurements with random noise SNRs of 2000, we identify maximum tropospheric and stratospheric layer widths that still lead to negligible transmission errors as, respectively, 0.6 and 2.0 km. The SNR of 2000 corresponds to considering transmission differences of 0.1% or greater as significant. Accordingly, our maximum layer width recommendations can vary depending on the SNR of the measurement, the band or transition of interest and the use of significantly different *a priori* VMR profiles (especially with markedly different gradients of VMRs). In particular, at polar or mountain sites, the VMR profiles of H₂O and O₃ can be markedly different than those in our study, as can be the SZA of observations. In any case, in practice one would strive to gradually transition from tropospheric layer widths in the region from 0 to 12 km, smoothly reaching stratospheric layer widths somewhere in the lower stratosphere, i.e. between 12 and 36 km, keeping in mind that the regions of gradients in temperature and VMR profiles should be well sampled by the discretization scheme.

While our main objective was to identify the maximum layer width in the troposphere and in the stratosphere in order to faithfully represent transmission spectra, we stress again that it was not to find the minimum number of layers in the forward model, or their optimal placement. Such a task would need a separate optimization for each target gas and IRWG observation station, and a consideration of other grid-related factors which may influence the subsequent retrieval step not considered in this study, e.g., abrupt changes in layer thickness.

Finally, based on this work we recommend that two side-by-side investigators engaged in an intercomparison study use identical discretization schemes in order to avoid creating transmission biases in the first iteration of their retrievals, with subsequent effects on the retrieved profiles. Furthermore, some of the narrow transmission biases induced by the different grid schemes can potentially be confounded with the effects of temperature- and pressure-dependent spectroscopic parameters that two side-by-side investigators may be attempting to derive from or confirm with their atmospheric measurements. Lastly, our study re-emphasizes the need to carefully consider the effect of broadly sloping transmission biases due to the wings of temperature-sensitive and interfering H₂O (or other) transitions; this can be accomplished with, e.g., retrieval parameters commonly used to fit background transmission level curvatures.

Acknowledgments

This work has been supported by NSERC, OGS, the Zonta International Foundation, the Joseph Bazylewicz Foundation, PREA, CFCAS, and the Marie Curie Mobility Actions. TAO was established with support from CFI, ORDCF, CRESTech, and the University of Toronto.

References

- [1] Kurylo MJ, Zander RJ. The NDSC—its status after ten years of operation. In: Proceedings of the XIXth quadrennial ozone symposium, Hokkaido University, Sapporo, Japan, 3–8 July 2000. p. 167–8.
- [2] Blumenstock T, Kopp G, Hase F, Hochschild G, Mikuteit S, Raffalski U, et al. Observation of unusual chlorine activation by ground-based infrared and microwave spectroscopy in the late Arctic winter 2000/01. *Atmos Chem Phys* 2006;6:897–905.
- [3] Wood SW, Batchelor RL, Goldman A, Rinsland CP, Connor BJ, Murcray FJ, et al. Ground-based nitric acid measurements at arrival heights, Antarctica, using solar and lunar Fourier transform infrared observations. *J Geophys Res* 2004;109(D18):D18307.
- [4] Velasco V, Notholt J, Warneke T, Lawrence M, Bremer H, Drummond JR, et al. Latitude and altitude variability of carbon monoxide in the Atlantic detected from ship-borne Fourier transform spectrometry, model, and satellite data. *J Geophys Res* 2005;110:D09306.
- [5] Schneider M, Blumenstock T, Chipperfield MP, Hase F, Kouker W, Reddmann T, et al. Subtropical trace gas profiles determined by ground-based FTIR spectroscopy at Izaña (28°N, 16°W): five-year record, error analysis, and comparison with 3-D CTMs. *Atmos Chem Phys* 2005;5:153–67.
- [6] Wiacek A, Jones NB, Strong K, Taylor JR, Mittermeier RL, Fast H. First detection of meso-thermospheric nitric oxide (NO) by ground-based FTIR solar absorption spectroscopy. *Geophys Res Lett* 2006;33:L03811.
- [7] Kasai YJ, Koshiro T, Endo M, Jones NB, Murayama Y. Ground-based measurement of strato-mesospheric CO by a FTIR spectrometer over Poker Flat, Alaska. *Adv Space Res* 2005;35:2024–30.
- [8] Zander R, et al. Secular trend and seasonal variability of the column abundance of N₂O above the Jungfraujoch station determined from IR solar spectra. *J Geophys Res* 1994;99(D8):16745–56.
- [9] Rinsland CP, et al. Multiyear infrared solar spectroscopic measurements of HCN, CO, C₂H₆, and C₂H₂ tropospheric columns above Lauder, New Zealand (45°S latitude). *J Geophys Res* 2002;107(D14):4185.
- [10] Rinsland CP, Zander R, Mahieu E, Chiou LS, Goldman A, Jones NB. Stratospheric HF column abundances above Kitt Peak (31.9°N latitude): trends from 1977 to 2001 and correlations with stratospheric HCl columns. *JQSRT* 2002;74:205–16.
- [11] Rinsland CP, et al. Long-term trends of inorganic chlorine from ground-based infrared solar spectra: past increases and evidence for stabilization. *J Geophys Res* 2003;108(D8):4252.
- [12] Yurganov LN, et al. Increased Northern Hemispheric carbon monoxide burden in the troposphere in 2002 and 2003 detected from the ground and from space. *Atmos Chem Phys* 2005;5:563–73.
- [13] Paton-Walsh C, Jones NB, Wilson S, Meier A, Deutscher N, Griffith DWT, et al. Trace gas emissions from biomass burning inferred from aerosol optical depth. *Geophys Res Lett* 2004;31:L05116.
- [14] Zhao Y, et al. Spectroscopic measurements of tropospheric CO, C₂H₆, C₂H₂, and HCN in northern Japan. *J Geophys Res* 2002;107(D18):4343.
- [15] Rinsland CP, Meier A, Griffith DWT, Chiou LS. Ground-based measurements of tropospheric CO, C₂H₆, and HCN from Australia at 34°S latitude during 1997–1998. *J Geophys Res* 2001;106(D18):20913–24.
- [16] Notholt J, et al. Enhanced upper tropical tropospheric COS: impact on the stratospheric aerosol layer. *Science* 2003;300(5617):307–10.
- [17] Dils B, et al. Comparisons between SCIAMACHY and ground-based FTIR data for total columns of CO, CH₄, CO₂ and N₂O. *Atmos Chem Phys* 2006;6:1953–76.
- [18] Sussmann R, Buchwitz M. Initial validation of ENVISAT/SCIAMACHY columnar CO by FTIR profile retrievals at the Ground-Truthing Station Zugspitze. *Atmos Chem Phys* 2005;5:1497–503.
- [19] Mahieu E, et al. Comparisons between ACE-FTS and ground-based measurements of stratospheric HCl and ClONO₂ loadings at northern latitudes. *Geophys Res Lett* 2005;32:L15S08.
- [20] Barret B, DeMazière M, Mahieu E. Ground-based FTIR measurements of CO from the Jungfraujoch: characterization and comparison with in situ surface and MOPITT data. *Atmos Chem Phys* 2003;3:2217–23.
- [21] Rodgers CD. *Inverse Methods for Atmospheric Sounding: Theory and Practice*. New Jersey: World Scientific Publishing Co. Pte. Ltd.; 2000.
- [22] Pougatchev NS, Connor BJ, Rinsland CP. Infrared measurements of the ozone vertical distribution above Kitt Peak. *J Geophys Res* 1995;100(D8):16689–97.
- [23] Rinsland CP, et al. Northern and southern hemisphere ground-based infrared spectroscopic measurements of tropospheric carbon monoxide and ethane. *J Geophys Res* 1998;103(D21):28197–217.
- [24] Barret B, DeMazière M, Demoulin P. Retrieval and characterization of ozone profiles from solar infrared spectra at the Jungfraujoch. *J Geophys Res* 2002;107(D24):4788.
- [25] Schneider M, Blumenstock T, Hase F, Höpfner M, Cuevas E, Redondas A, et al. Ozone profiles and total column amounts derived at Izaña, Tenerife Island, from FTIR solar absorption spectra, and its validation by an intercomparison to ECC-sonde and Brewer spectrometer measurements. *JQSRT* 2005;91:245–74.
- [26] Wiacek A, Taylor JR, Strong K, Saari R, Kerzenmacher TE, Jones NB, et al. Ground-based solar absorption FTIR spectroscopy: a novel optical design instrument at a new NDSC Complementary Station, characterization of retrievals and first results. *J Atmos Oceanic Technol* 2007;24:432–48.
- [27] Connor BJ, Jones NB, Wood SW, Keys JG, Rinsland CP, Murcray FJ. Retrieval of HCl and HNO₃ profiles from ground-based FTIR data using SFIT2. In: Proceedings of the XVIIIth quadrennial ozone symposium, L'Aquila, Italy, 12–21 September 1996. p. 485–8.

- [28] Hase F, Hannigan JW, Coffey MT, Goldman A, Höpfner M, Jones NB, et al. Intercomparison of retrieval codes used for the analysis of high-resolution, ground-based FTIR measurements. *JQSRT* 2004;87:25–52.
- [29] Rinsland CP, Boughner RE, Larsen JC, Stokes GM, Brault JW. Diurnal variations of atmospheric nitric oxide: ground-based infrared spectroscopic measurements and their interpretation with time-dependent photochemical model calculations. *J Geophys Res* 1984;89(D6):9613–22.
- [30] Notholt J, Toon GC, Lehmann R, Sen B, Blavier JF. Comparison of Arctic and Antarctic trace gas column abundances from ground-based Fourier transform infrared spectrometry. *J Geophys Res* 1997;102(D11):12863–9.
- [31] Toon GC, Blavier JF, Sen B, Salawitch RJ, Osterman GB, Notholt J, et al. Ground-based observations of Arctic O₃ loss during spring and summer 1997. *J Geophys Res* 1999;104(D21):26497–510.
- [32] Rinsland CP, Goldman A, Stephen TM, Chiou L, Mahieu E, Zander R. SF₆ ground-based infrared solar absorption measurements: long-term trend, pollution events, and a search for SF₅CF₃ absorption. *JQSRT* 2003;78:41–53.
- [33] Griffith DWT, Jones NB, McNamara B, Paton-Walsh C, Bell W, Bernardo C. Intercomparison of NDSC ground-based solar FTIR measurements of atmospheric gases at Lauder, New Zealand. *J Atmos Oceanic Technol* 2003;20:1138–53.
- [34] Meier A, Goldman A, Manning PS, Stephen TM, Rinsland CP, Jones NB, et al. Improvements to air mass calculations for ground-based infrared measurements. *JQSRT* 2004;83:109–13.
- [35] Barret B, Hurtmans D, Carleer MR, DeMazière M, Mahieu E, Coheur PF. Line narrowing effect on the retrieval of HF and HCl vertical profiles from ground-based FTIR measurements. *JQSRT* 2005;95:499–519.
- [36] Rinsland CP, Goldman A, Elkins JW, Chiou LS, Hannigan JW, Wood SW, et al. Long-term trend of CH₄ at northern mid-latitudes: comparison between ground-based infrared solar and surface sampling measurements. *JQSRT* 2006;97:457–66.
- [37] Schneider M, Hase F, Blumenstock T. Water vapour profiles by ground-based FTIR spectroscopy: study for an optimised retrieval and its validation. *Atmos Chem Phys* 2006;6:811–30.
- [38] Yamamori M, Kagawa A, Kasai Y, Mizutani K, Murayama Y, Sugita T, et al. Validation of ILAS-II version 1.4 O₃, HNO₃, and temperature data through comparison with ozonesonde, ground-based FTS, and lidar measurements in Alaska. *J Geophys Res* 2006;111:D11S08.
- [39] Griesfeller A, Griesfeller J, Hase F, Kramer I, Loës P, Mikuteit S, et al. Comparison of ILAS-II and ground-based FTIR measurements of O₃, HNO₃, N₂O, and CH₄ over Kiruna, Sweden. *J Geophys Res* 2006;111:D11S07.
- [40] Rothman LS, et al. The HITRAN 2004 molecular spectroscopic database. *JQSRT* 2005;96:139–204.
- [41] Meier A, Toon GC, Rinsland CP, Goldman A, Hase F. Spectroscopic atlas of atmospheric microwindows in the middle infra-red, 2nd ed. IRF Technical Report 048 ISSN 0284-1738, Swedish Institute of Space Physics; 2004.
- [42] Gallery WO, Kneizys FX, Clough SA. Air mass computer program for atmospheric transmittance/radiance calculation: FSCATM. Environmental Research Papers No. 828 (AFGL-TR-83-0065), Air Force Geophysics Laboratory; 1983.
- [43] Rothman LS, et al. The HITRAN molecular spectroscopic database and HAWKS (HITRAN Atmospheric Workstation): 1996 edition. *JQSRT* 1998;60:665–710.
- [44] Notholt J, Toon G, Jones N, Griffith D, Warneke T. Spectral line finding program for atmospheric remote sensing using full radiation transfer. *JQSRT* 2006;97:112–25.
- [45] Fischer J, Gamache RR, Goldman A, Rothman LS, Perrin A. Total internal partition sums for molecular species in the 2000 edition of the HITRAN database. *JQSRT* 2003;82:401–12.
- [46] Reisinger AR, Jones NB, Matthews WA, Rinsland CP. Southern hemisphere midlatitude ground-based measurements of ClONO₂: method of analysis, seasonal cycle, and long term-trend. *J Geophys Res* 1995;100(D11):23183–94.